1 **Geochemical evidence for regional and long-term topography-driven**

2 **groundwater flow in an orogenic crystalline basement (Aar Massif,**

3 **Switzerland)**

4

5 **Christoph Wanner[1*], H. Niklaus Waber[1], Kurt Bucher[2]**

6 *[1]Rock-Water Interaction Group, Institute of Geological Sciences, University of Bern,*

7 *Baltzerstrasse 3, CH-3012 Bern, Switzerland*

8 **corresponding author (wanner@geo.unibe.ch)*

9 *[2]Mineralogy and Petrology, University of Freiburg, Albertstr. 23b, D-79104 Freiburg,*

10 *Germany*

11

12 **ABSTRACT**

13   Detailed knowledge about the circulation of meteoric water in non-magmatic, orogenic

14 belts is fundamental for assessing the potential of such settings for geothermal power

15 production, as well as their use as potential groundwater resources. To get more general

16 insight into these hydrological processes, we have conducted regional (20 x 10 x 9 km)

17 thermal-hydraulic-chemical (THC) simulations of meteoric water circulation in the orogenic,

18 crystalline basement of the Aar Massif in the Central Alps, Switzerland. Model results were

19 compared to numerous geochemical and isotopic analyses of groundwater discharging into

20 the longest and deepest tunnel of the world, the Gotthard railbase tunnel located within the

21 model domain. Explicitly considering the surface topography in our model was sufficient to

22 reproduce all key characteristics of the tunnel inflows (salinity, temperature, δ^{18}O values, and

23 up- and downward directed flow zones inferred from geochemical constraints). This

24 quantitatively confirms that surface topography operates as the governing control on fluid

25 flow in orogenic crystalline basements with meteoric water infiltration occurring at high

26 altitude and resulting upward directed flow zones along major valleys. Owing to low flow

27 rates below 2 m year^{-1}, computed residence times of the longest flow paths were above 100 k

years, confirming that groundwater and/or porewater in orogenic crystalline basements may act as an archive for palaeohydrologic variations. Moreover, simulation results show that down to the lower model boundary at 9 km depth, penetration of meteoric water is not limited by the decrease in permeability with depth that is typically observed in granitic rocks. This suggests that advective fluid transport in orogenic crystalline basements may reach the brittle-ductile transition zone and that infiltrating meteoric water can attain temperatures well above 150 °C. We conclude that orogenic geothermal systems are promising plays for geothermal power production.

1. Introduction

Fluid flow in crystalline basements is enabled by the occurrence of interconnected fracture networks (Stober and Bucher, 2007; Bucher and Stober, 2010) and the presence of hydrological driving forces (Ingebritsen and Manning, 1999). Although mountain topography has been long ago recognized as key driver for meteoric water circulation in non-magmatic, orogenic belts (e.g. Hubbert, 1940; Forster and Smith, 1988; Ge et al., 2008, Goderniaux et al., 2013), direct observations linking downward and upward directed flow zones are still sparse. On the one hand, numerous studies have described the ascent of meteoric water along deep-reaching faults (i.e. along permeability anomalies) based on the occurrence of thermal springs and their chemical and isotopic composition. Examples include sites in the Canadian Rocky Mountains (Grasby et al., 2016), the Southern Alps of New Zealand (Reyes et al., 2010), the central European Alps (Pfeifer et al., 1992; Sonney and Vuataz, 2008; Diamond et al., 2018), the Black Forest (Stober et al., 1999; Stober and Bucher, 2015), the Pyrenees (Taillefer et al., 2018), the Himalayas (Craw et al., 2005), and locations in China (Bucher et al., 2009; Stober et al., 2016). Other manifestations of ascending fluids include fossil hydrothermal breccias (Hofmann et al., 2004), and positive temperature anomalies (i.e. above

those predicted by the local geothermal gradient) recorded along shallow tunnels and boreholes (Pastorelli et al., 2001; Valla et al., 2016). On the other hand, shallow (<2 km) infiltration of meteoric water into crystalline rocks is evidenced by the occasional occurrence of large inflows (>100 L s^{-1}) of cold meteoric water into highway or railway tunnels, associated with negative temperature anomalies (Hunziker et al., 1990; Maréchal et al., 1999; Pastorelli et al., 2001). The maximum penetration of meteoric water, however, is still under debate and suggested depths range from 5 to 23 km (Diamond et al., 2018, and references therein). The rheology of the continental crust changes with increasing depth from brittle to ductile deformation behavior. Below the brittle-ductile transition zone located in a depth of about 12–14 km at a typical crustal geothermal gradient of 25–30 °C km^{-1} (Wintsch et al. 1995; Stober and Bucher, 2007), Darcy-flow is not possible (Stober and Bucher, 2015) and other transport mechanisms are responsible for fluid transfer through the ductile crust (Connolly and Podladchikov, 2015). Thus, the studies reporting the greatest depths invoke penetration of meteoric water below the brittle-ductile transition zone (Wickham et al., 1993; Cartwright and Buick, 1999). The large range in postulated penetration depths, however, may also be inherited from a variation in methodology ranging from stable water isotope analyses of minerals and fluid inclusions in hydrothermal rocks to solute geothermometry and geochemical modeling applied to thermal springs, and does not necessary imply penetration below the brittle-ductile transition zone (see Diamond et al., 2018 and references therein). In any case, it reflects the limited knowledge about structural controls on meteoric water infiltration into crystalline basements and on how infiltration zones are actually connected to deep-reaching fault zones, along which meteoric water can again reach the surface and discharge as thermal springs eventually (Belgrano et al., 2016). This forms a particular challenge for assessing orogenic, crystalline basements as potential groundwater resources (Ge et al., 2008), and for evaluating their potential for geothermal power production (Wanner et al., 2019).

Here we present results from regional 3D (20 x 10 x 9 km) thermal-hydraulic-chemical (THC) simulations of fluid flow in the Aar Massif in the Central Alps, Switzerland.

The study area constitutes an ideal site to get more insight into regional hydrogeological processes in orogenic crystalline basements because, (i) numerous chemical and isotopic analyses of water inflows along the World's longest and deepest tunnel, the Gotthard railbase tunnel (Bucher et al., 2012) provide a unique opportunity to study such processes, (ii) the area includes both major valleys as well as mountain peaks, which appear to correlate with distinct upward and downward directed flow zones at the tunnel level, and (iii) major (i.e. regional) structural and thermal anomalies are absent. Thus, with these specifications the study area allows to particularly assess the role of topography as a control of fluid flow in orogenic crystalline basements. To overcome the shortage of hydraulic measurements in this regional system, we use the available chemical and isotopic data to constrain our model and to quantitatively evaluate whether mountain topography indeed operates as the first order driving force for regional meteoric water circulation.

2. Geological and hydrogeological setting

The 57 km long Gotthard rail base tunnel crosses the Central Alps at a base level of ca. 500 m a.s.l. The construction was simultaneously carried out in five individual sections, which was enabled by drilling vertical access shafts. Our study exclusively deals with the Amsteg section of the tunnel, corresponding to a 11.5 km long section in the northern part of the tunnel (Fig. 1), because only for this tunnel section groundwater inflows were systemically sampled with a high spatial resolution during construction. The construction took place between 2003 and 2006 using a 400 m long tunnel-boring machine.

The geology and hydrogeology of the Aar Massif as well as the Amsteg section of the tunnel have been previously described in detail and are summarized in the following. The section crosscuts the crystalline basement of the Aar Massif, which represents a major NE-SW striking complex of the Variscan basement (120 x 20 km in size). The Aar Massif was overprinted by Alpine greenshist-type metamorphism and associated deformation (Abrecht, 1994; Schaltegger, 1994; Labhart, 1999). The different geological units exposed along the

Amsteg section are made of granites, gneisses, and volcanic rocks (e.g. metarhyolites) (Bucher et al., 2012). Mineralogically, these rocks have similar compositions and are dominated by quartz, albite, K-feldspar and chlorite, minor amounts of biotite and muscovite, and accessory pyrite and calcite (Bucher et al., 2012). The thickness of the rock column above the tunnel is between 300 and 2200 m (Fig. 2).

North–South compression during the Alpine orogeny resulted in steeply dipping geological units and E–W trending foliation (Steck and Hunziker, 1994). Brittle deformation caused by exhumation of the Aar Massif and subsequent cooling formed shear fractures and joint systems (Choukroune and Gapais, 1983; Laws et al., 2003). High deformation zones currently strike parallel to the geological units and steeply dip to the S or N (Laws et al., 2003). Thus, the tunnel crosscuts the steeply dipping units and the nearly vertical fracture system at an angle close to 90 degree (Fig. 2). Based on a hydraulic test performed in a zone with major water inflows in the nearby Sedrun section of the tunnel (Fig. 1), the hydraulic conductivity in such highly deformed zones may be as high as 10^{-6} m s^{-1} (Bucher et al., 2012). In turn, the geometric mean of the hydraulic conductivity across the entire Sedrun section ranges from 3 to 6 x 10^{-9} m s^{-1} (Masset and Loew, 2013).

During drilling of the Amsteg section, 122 groundwater samples were collected from water conducting fractures before these were permanently sealed with concrete. Owing to the induced pressure drop, the water inflow rate from individual fractures ranged from 0.0004 to 6 L s^{-1}. Full chemical analyses were performed on all 122 groundwater samples with the results being reported in Bucher et al. (2012). Groundwater from the various inflows range from freshwater to strongly mineralized water (TDS = 171–3231 mg L^{-1}). Their chemical composition varies from the general Na-CO$_3$ and Na-SO$_4$ chemical types up to about 700 mg L^{-1} total mineralization to the general Na-Cl chemical type at elevated mineralization (>700 mg L^{-1}). All samples are characterized by an alkaline *pH* ranging from 8.3 to 10.4. In their chemical characteristics, the groundwater samples from the Gotthard railway tunnel thus resemble many other crystalline groundwaters of similar total mineralization (e.g. Nordstrom et al. 1989, Pearson et al. 1991, Waber et al. 2017, Schneeberger et al. 2019). The chemical

composition is inherited from water-rock interaction reactions between infiltrating meteoric water and the granitic mineralogy of the crystalline basement. Beside such advective reactive transport along interconnected fracture networks (i.e. the fracture porosity), there are strong indications for a diffusive uptake of mainly Cl, Na, SO_4, Li, and Br from porewater present in the intact, non-fractured, and low permeable rock matrix (i.e. the matrix porosity). This porewater presumably constitutes a remnant of a hydrothermal fluid that evolved during alpine metamorphism (Seelig and Bucher, 2010; Wanner et al., 2017). The important role of matrix porewater on the chemical and isotopic composition of groundwater in crystalline settings originates from strong concentration gradients between fracture groundwater and matrix porewater that are continuously balanced by (mainly) diffusion over time (Waber et al., 2012).

The surface hydrology above the Amsteg section of the tunnel is controlled by the catchment of the Maderaner Valley including the Etzli side Valley (Fig. 1). At the town of Amsteg, the two valleys drain into the Reuss, a major alpine river in Switzerland, at an average annual discharge of 9 m^3 s^{-1} (FOEN, 2015). The average annual precipitation rates in the catchment are altitude dependent and range from 1200 mm at 500 m a.s.l. to 1500 mm above 2000 m a.s.l. (MeteoSwiss, 2019).

3. Constraints from geochemical data

Among the numerous physical and chemical parameters reported for groundwater samples collected along the Amsteg section (Bucher et al., 2012), the temperature, *pH*, as well as the concentrations of Cl and Si are particularly useful to constrain our THC simulations as described below. In addition to the published chemical analyses, in this study we carried out analyses of the stable isotopes of the water molecule on 30 out of the 122 groundwater samples collected along the Amsteg section. All these geochemical constraints contribute to establishing a conceptual model of the hydrodynamic functioning of the pre-tunnel stage of the studied crystalline massif and they serve to constrain our THC model as described below.

3.1. Stable water isotopes

167

168   Stable isotopes of water, expressed as $\delta^{18}O$ and δ^2H in per mil (‰) relative to

169   VSMOW, were analyzed at the Institute of Geological Sciences, University of Bern, by

170   isotope ratio infrared spectroscopy (IRIS) using a Picarro L2120-i cavity ring down

171   spectrometer (CRDS) with vaporization module V1102-i, coupled to an HTC PAL auto-

172   sampler (CTC Analytics). Post-run correction of oxygen and hydrogen stable isotope

173   measurements was conducted according to van Geldern and Barth (2012). The analytical error

174   (1σ) was ± 0.1‰ for $\delta^{18}O$ and ± 1.0‰ for δ^2H based on multiple measurements of internal

175   and IAEA standards. Duplicate analyses agreed well within this error. In contrast to the

176   immediately conducted chemical analyses (Bucher et al., 2012), those of the stable water

177   isotopes was performed up to 10 years after the samples were collected during construction of

178   the Amsteg section (2003–2006). To test whether evaporation occurred during sample

179   storage, the concentrations of major cations and anions (Cl^-, Na^+, and SO_4^{2-}) were re-

180   measured at the Institute of Geological Sciences, University of Bern by ion chromatography

181   using a Metrohm ProfIC AnCat MCS IC system. The analytical uncertainty was better than ±

182   5% based on multiple measurements of high-grade, commercial standard solutions.

183   Since evaporation was identified, measured $\delta^{18}O$ and δ^2H values were corrected as

184   described in the Supporting Information. Measured and evaporation-corrected values are both

185   listed in Table S1 (Supporting Information) together with the re-measured ion concentrations.

186   Compared to the ion concentrations reported in Bucher et al. (2012), our groundwater samples

187   showed an increase of up to 15 % corresponding to the evaporated fraction of the original

188   sample volume. The corrected $\delta^{18}O$ and δ^2H values plot on the global and local meteoric

189   water lines (GMWL, LMWL) (Fig. 3), demonstrating that all groundwater samples originate

190   from meteoric water that has infiltrated at the surface.

191   Along the Amsteg section, $\delta^{18}O$ and δ^2H values of our groundwater samples do not

192   show any particular spatial trend (Fig. 2b). This is likely due to the fact that they represent a

193   homogenized (i.e. "averaged") isotope signature of meteoric water infiltrated at different

194   altitudes and different times in the past. The latter is relevant because the residence time of

195   meteoric water circulating in the Aar Massif is substantial and may reach several 10 k years

196   such as demonstrated by the lack of detectable ^{14}C in meteoric water penetrating up to 10 km

197   deep before discharging as thermal springs below Grimsel Pass also located within the Aar

198   Massif (Waber et al., 2017; Diamond et al., 2018). Thus, the main constraint from stable

199   isotope analysis for our model is that all groundwater samples discharging at the tunnel level

200   originate from meteoric water that has infiltrated at the surface at some point in the past.

201   Moreover, given that our groundwater $\delta^{18}O$ and δ^2H values are well within the range of

202   current precipitation in the Aar Massif (e.g. meteorological stations Grimsel and Guttannen,

203   FOEN, 2014) (Fig. 3), infiltration has mainly occurred during times where the average

204   climatic conditions were similar to those in the current Holocene interglacial period (<11.5

205   ka). In turn, infiltration was limited or even absent during cold temperature periods and the

206   glacial cycles because this would have likely resulted in $\delta^{18}O$ and δ^2H values at the lower

207   limit or even outside the range of current precipitation (Fig. 3). This is consistent with recent

208   hydrogeological investigations of similar crystalline massifs in France, for which it was

209   suggested that infiltration at high altitude mainly occurred during the Holocene interglacial

210   period, while it was much lower during the preceding glaciation period (Maréchal et al., 1999;

211   Thiebaud et al., 2010; Dzikowski et al., 2016). Hence, the subsurface residence time of

212   meteoric water in our model is constrained to Holocene times (<11.5 ka) or similar

213   interglacial periods in the past such as the Eemian interglacial dated between about 130–115

214   ka (Preusser et al., 2011).

215

216   **3.2. Physico-chemical evolution of tunnel inflows along the Amsteg section**

217

218   **3.2.1. Saturation state of chalcedony and quartz**

219   Bucher et al. (2012) have suggested that for "low" *pH* tunnel inflows (*pH* < 9), the

220   dissolved silica concentration is mainly controlled by the solubility of chalcedony, whereas

221   above *pH* 9.5 it is controlled by quartz. Calculating the saturation state of chalcedony in

222   groundwater samples of *pH* < 9.5 and of quartz in those of *pH* > 9.5, using TOUGHREACT

223   V3 (Xu et al., 2014) in combination with the Soltherm.H06 database (Reed and Palandri,

224   2006), demonstrates that most groundwater samples are near saturation or slightly under-

225   saturated with respect to the silica-controlling phase (saturation index $S.I.$ = - 0.4 to + 0.1)

226   (Fig. 2c). The only exceptions are tunnel inflows collected beneath the only major valley

227   along the Amsteg section, the Maderaner Valley at ca. 9 km along the tunnel, which show a

228   significant supersaturation ($S.I.$ > 0.1) with respect to chalcedony (Figs. 2a, c). Owing to the

229   lower solubility of quartz, this would also be the case if these samples were solubility

230   controlled by quartz instead of chalcedony despite showing pH values below 9.5.

231   Supersaturation with respect to quartz and/or chalcedony is a common feature of thermal

232   waters and it is observed due to (i) the solubility decrease associated with the decrease in

233   temperature upon ascent and cooling of thermal fluids, and (ii) slow precipitation kinetics of

234   quartz and chalcedony in combination with fast upflow (Wanner et al., 2014; Diamond et al.,

235   2018). Thus, based on the observed supersaturation, there is strong geochemical evidence that

236   the groundwater samples collected beneath the Maderaner Valley have experienced

237   temperatures above the discharge temperature and hence have infiltrated into the tunnel from

238   below (Fig. 2a). While we do not attempt to reconstruct the calculated saturation indices, the

239   upflow directed flow zone proposed to occur below the Maderaner Valley serves as important

240   constraint for our model.

241

242   **3.2.2. Cl concentration profile**

243   The Cl concentration profile along the Amsteg section shows a distinct peak with a

244   maximum concentration of 1300 mg L^{-1} at about 10 km along the tunnel where it intersects a

245   volcanoclastic unit called Intschi zone (Figs. 2a, d). The peak is located roughly 1 km south of

246   the location where the tunnel crosses the Bristen Granite beneath the lowest point of the

247   Maderaner Valley and where the Cl concentration in the groundwater is around 400 mg L^{-1}.

248   Plotting the Cl concentrations against the discharge temperature (Fig. 4a) demonstrates that

249   groundwater samples collected along the Amsteg section fall into two distinct groups. With

250   the exception of two outliers, the first group consists of all samples collected up to a distance

251 of 11.5 km along the tunnel. In these samples, Cl and the discharge temperature are linearly

252 correlated and include all samples forming the Cl peak discussed above. The second group

253 includes the samples at a distance greater than 11.5 km along the tunnel. These samples are

254 characterized by generally low Cl concentrations (< 200 mg L^{-1}) that are not correlated with

255 the discharge temperature.

256   Since elevated Cl concentrations such as in case of the first group (<11.5 km) are

257 consistent with longer flow paths and continuous uptake of solutes from the postulated

258 ancient porewater source (Seelig and Bucher, 2010; Bucher et al., 2012; Wanner et al., 2017),

259 we suggest that all groundwater samples of the first group (<11.5 km) have infiltrated from

260 below, although only the ones collected beneath the lowest point of the Maderaner Valley

261 show evidence for temperatures above the discharge temperature based on the calculated

262 silica phase saturation indices (Fig. 2c). For groundwater samples with low Cl concentrations

263 such as in case of the second group, we suggest that they have infiltrated into the tunnel from

264 above. This is consistent with results from reactive transport modeling (Wanner et al., 2017)

265 showing that the composition of groundwater samples with very low Cl concentrations (<3

266 mg L^{-1}) and collected at about 15 km beneath the highest peak of the Amsteg section, the

267 Chrüzlistock, can be explained by a rather simple 1D reactive transport model considering the

268 reaction of infiltrating meteoric water with the granitic mineralogy only (Wanner et al., 2017).

269 Consequently, these particular samples have likely infiltrated into the tunnel from above,

270 consistent with shorter residence times and essentially no uptake of Cl from the postulated

271 ancient porewater source. Owing to their low Cl concentrations and based on the temperature

272 vs. Cl plot (Fig. 4a), the same downward directed flow may apply for all groundwater

273 samples belonging the second group of samples (>11.5 km).

274   The upflow and downflow directed flow zones identified from the spatial correlation

275 between geochemical properties of the collected groundwater samples and surface topography

276 (Fig. 2a) will serve as calibration target for our model. Moreover, since Cl likely originates

277 from an ancient porewater source (Seelig and Bucher, 2010; Wanner et al., 2017), Cl is used

278   as a residence time tracer in our model and the Cl concentration profile recorded along the

279   Amsteg section (Fig. 2d) will also serve as constraint for our model.

280

281   **3.2.3. Temperature profile**

282   The temperature of the groundwater samples collected along the Amsteg section closely

283   follows the surface topography (Figs. 2a, e). In fact, the correlation between temperature and

284   overburden is strongly linear and nearly perfect (Fig. 4b). Taking into account the

285   supersaturation with respect to chalcedony and quartz calculated for groundwater samples

286   collected beneath the Maderaner Valley (Fig. 2c), this observation suggests that the upflow

287   rate of the proposed upward directed flow zone is too low to generate any temperature

288   anomaly (i.e. temperatures above those predicted by the local geothermal gradient). Together

289   with the observed tunnel inflow rates, the recorded temperature profile will serve as constraint

290   in our model.

291

292   **3.3. Correlations in groundwater samples collected along the Bristen Granite**

293   Groundwater samples collected where the tunnel intersects the Bristen Granite beneath

294   the Maderaner Valley (ca. 9 km along the tunnel) show strong linear correlations between

295   major as well as minor solutes and Cl, and between δ^{18}O and Cl (Fig. 5). Such correlations are

296   typical manifestations of binary fluid mixtures. Elevated Cl, Na, SO_4, Li, and Br

297   concentrations (Wanner et al., 2017) as well as the small tunnel overburden of about 300 m

298   (Fig. 2a) indicating elevated permeability (Fig. 6), suggest that these groundwaters represent a

299   binary mixture between an ascending, highly-mineralized fluid endmember and dilute

300   meteoric water originating from the surface such as demonstrated for other locations within

301   the Aar Massif (Diamond et al., 2018). Significant admixture of dilute meteoric water to the

302   ascending fluid endmember is consistent with the observation that the maximum tunnel

303   inflow rate (6 L s^{-1}) was recorded at this particular location of the tunnel. Moreover, it is

304   consistent with the negative linear correlation observed between δ^{18}O and Cl (Fig. 5c),

305 suggesting that the diluting meteoric water (low Cl, high $\delta^{18}O$) has infiltrated at a lower

306 altitude than the deep fluid endmember (high Cl, low $\delta^{18}O$), for instance at the bottom of the

307 Maderaner Valley at about 800 m a.s.l. In turn, this interpretation implies that the ascending

308 fluid endmember has originally infiltrated at an altitude that is above the Maderaner Valley

309 before eventually discharging into the tunnel from below. In addition to low $\delta^{18}O$, this results

310 in longer residence times and more Cl uptake from the proposed porewater source yielding

311 elevated Cl concentrations, eventually (Fig. 2d). The Cl uptake, however, is not accompanied

312 by a shift of $\delta^{18}O$ values away from the GMWL towards less negative values, despite that

313 matrix porewater collected within the Aar Massif as well as ancient metamorphic fluids

314 trapped in fluid inclusions show elevated $\delta^{18}O$ and $\delta^{2}H$ values (Mullis et al., 1994,

315 Schneeberger et al., 2019; Fig. 3). Compared to Cl, the shift in $\delta^{18}O$ (and likewise $\delta^{2}H$) is

316 limited because (i) infiltrating meteoric water has a very high H_2O concentration of 55.6 mol

317 L^{-1} (i.e. $[H_2O] = 1$ kg L^{-1} at $T = 4$ °C), (ii) the isotopic signature of infiltrating meteoric water

318 covers a large range that does not substantially differ from the range of expected porewater

319 (Fig. 3), and (iii) the concentration gradient controlling diffusive uptake of heavy $\delta^{18}O$ is

320 given by the gradient of the $^1H_2^{18}O$ and $^1H_2^{16}O$ isotopologues (i.e. same molecule but different

321 mass), which are in the per mil range per distant unit only. In case of Cl, the low

322 concentrations of infiltrating meteoric water (µM range) as well as the strong concentration

323 gradient (M range per distant unit) result in a significantly higher uptake from the ancient

324 porewater source. While fully assessing the causes for the missing $\delta^{18}O$ shift is beyond the

325 scope of the present work, its absence is consistent with analyses of mineralized thermal

326 springs collected within the Aar Massif (Diamond et al., 2018) and groundwater samples

327 collected from the nearby Gotthard highway tunnel (Pastorelli et al., 2001). In any case, the

328 absence of observable $\delta^{18}O$ shifts during meteoric water circulation forms an important

329 constraint in our model.

330   The identified admixture of cold meteoric water implies that the Cl and Si concentrations

331 and hence the silica supersaturation of the deep fluid endmember ascending where the tunnel

332   intersects the Bristner Granite beneath the Maderaner Valley at about 9 km along the tunnel is

333   actually higher than the obtained values (Figs. 2c, d). Thus, without dilution with meteoric

334   water possibly caused by the tunnel construction work, the peak in the Cl profile (Fig. 2d)

335   might have actually occurred there and not as currently observed at about 10 km where the

336   tunnel intersects the volcanoclastic Intschi zone (Fig. 2a). The correlations identified for the

337   Bristen Granite groundwaters samples, however, fail to match the corresponding parameters

338   of the Intschi zone (Fig. 5). This demonstrates that the two units are not directly linked

339   hydrologically, although they both lie within the upward directed flow zone postulated to

340   occur at a distance <11.5 km along the tunnel (Fig. 2a). The absence of a direct flow

341   connection between the two units serves as additional constraint for our model.

342

343   **4. Model setup**

344   Our forward thermal-hydraulic-chemical simulations aim to assess the role of surface

345   topography on controlling regional meteoric water circulation in orogenic crystalline

346   basements. Therefore, simulations were performed for a large 3D domain (20 x 10 x 9 km)

347   including the entire Amsteg section of the Gotthard railbase tunnel, and by explicitly

348   considering the surface topography combined with stable water isotopes.

349

350   **4.1. Numerical model**

351   All simulations were performed using TOUGHREACT V3 (Xu et al., 2014), a well-

352   established integral finite difference code for modeling coupled thermo-hydrodynamic-

353   chemical processes in geothermal and volcanic systems (e.g., Wanner et al., 2014). All

354   simulations were performed using equation-of-state EOS1, which simulates water and

355   coupled heat flow in the single-phase state according to the mass balance equation

356

357   $$\frac{\partial M_{W,H}}{\partial t} = -\nabla F_{W,H} + q_{W,H}$$ (1)

358

359 where $M_{W,H}$ is the accumulation term for water M_W (kg m^{-2}) or heat M_H (J m^{-2}), $q_{W,H}$ are water

360 or heat sinks (-) or sources (+) and $F_{W,H}$ refers to the water flux F_W (kg m^{-2} s^{-1}) or heat flux F_H

361 (J m^{-2} s^{-1}). For fully saturated, single-phase flow problems F_W is equal to the Darcy flux u (m

362 s^{-1})

363 $$u = -\frac{k}{\mu}(\nabla P - \rho g) \qquad (2)$$

364

365 where k is the intrinsic permeability (m^2), μ is the water viscosity (Pa s), ∇P (Pa m^{-1}) is the

366 water pressure gradient with respect to distance (i.e., hydraulic head differential), ρ is the

367 density of water (kg m^{-3}) and g is the acceleration due to gravity (m s^{-2}). Heat flux F_H (J m^{-2} s^{-}

368 ^{1}) is defined as

369

370 $$F_H = C_M \times T \times \rho_M \times u - \lambda \times \nabla T \qquad (3)$$

371

372 where C_M (J kg^{-1} K^{-1}) and ρ_M (kg m^{-3}) are the specific heat capacity and the density of the

373 porous medium (rock + porewater), T (K) is the temperature of the porous medium (i.e. rock

374 and water), λ is the thermal conductivity of the wet rock (J s^{-1} m^{-1} K^{-1} = W m^{-1} K^{-1}), and ∇T

375 (K m^{-1}) is the gradient in temperature between adjacent grid blocks. The porous medium

376 parameters ρ_M and C_M are calculated as

377

378 $$\rho_M = (1 - \phi) \times \rho_R + \phi \times \rho_W \qquad (4)$$

379 $$C_M = (1 - \phi) \times C_R + \phi \times C_W \qquad (5)$$

380

381 where the subscripts $_R$ and $_W$ denote the corresponding rock and water values, respectively,

382 and ϕ is the porosity. Equation EOS1 calculates the temperature dependence of water

383 properties (e.g., density, specific enthalpy and viscosity) from the steam table equations given

384 by the International Formulation Committee (1967).

385

4.2. Model geometry

Along the Amsteg section, the surface topography is mainly shaped by the Maderaner Valley and the surrounding mountain peaks. Therefore, the horizontal extent of the model was constrained by the catchment of the Valley covering an area of about 20 x 10 km (Figs. 1, 7). This means that the southernmost part of the Amsteg section was not simulated. The upper model boundary was defined by numerically shaping an initially regular mesh with a digital elevation model (DEM) of the area using the "fit surface" PyTOUGH method (Croucher, 2015). Such approach eventually created an irregular mesh with a horizontal resolution of 250 x 250 m. The altitude of the lower model boundary was somewhat arbitrarily set to -5400 m a.s.l. to allow fluid circulation below the tunnel. The vertical extent of the grid blocks gradually increased from 150 m near the surface to a maximum extent of 600 m at altitudes below 0 m a.s.l., yielding a total of about 82,000 grid blocks.

In the absence of transmissivity, as well as fracture connectivity, spacing, and aperture data, and under consideration of the large model domain (20 x 10 x 9 km) the complex interconnected, hydraulically active fracture network was conceptionalized as a single (i.e. homogenously fractured) rock continuum, where the assigned porosity refers to the fracture porosity of the entire rock volume. This means that our simulations do not explicitly distinguish between advective flow along the hydraulically active fracture network of the Aar Massif and the diffusive and conductive interaction with the adjacent intact rock matrix. Similarly, since our model aims at unraveling the regional flow system, the model does not explicitly include the tunnel. As such, the model neglects the pressure drop induced by the tunnel and simulation results refer to the pre-tunnel stage of the system.

4.3. Simulating the fate of stable water isotopes and the continuous uptake of Cl

The main benefits of using a fully coupled THC simulator such as TOUGHREACT are (i) to include the transport of stable water isotopes in terms of a water source tracer in our simulations and (ii) to adopt the continuous uptake of Cl from the proposed porewater source (Seelig and Bucher, 2010; Wanner et al., 2017). The fate of the three most abundant stable

414   water isotopologues ($^1H_2^{16}O$, $^1H_2^{18}O$, $^1H^2H^{16}O$), corresponding to a cumulative abundance of

415   >99.9 %, was simulated following the approach described by Singleton et al. (2005). To do

416   so, $^1H_2^{18}O$ and $^1H^2H^{16}O$ were defined as primary species with distinct total concentrations in

417   addition to the $^1H_2^{16}O$ species used by default. This allows calculating δ^2H and $\delta^{18}O$ values

418   from the modeled $[^1H^2H^{16}O]/[^1H_2^{16}O]$ and $[^1H_2^{18}O]/[^1H_2^{16}O]$ total concentration ratios

419   ($R_{modeled}$)

420

421    $$\delta = \left(\frac{R_{modeled}}{R_{SMOW}} - 1\right) \times 1000 \qquad (6)$$

422

423   where R_{SMOW} refers to the corresponding ratios in standard mean ocean water (SMOW). For

424   our simulations, δ^2H and $\delta^{18}O$ values were fixed at the upper model boundary to define

425   altitude dependent values for the infiltrating meteoric water and to use them as water source

426   tracer. In the absence of historical rainwater data, the actual $\delta^{18}O$ values were constrained by

427   the long-term $\delta^{18}O$ monitoring of current rainwater collected along the nearby Grimsel

428   transect yielding an average value of -13.25 ‰ at 1980 m a.s.l. (i.e. at the Grimsel station)

429   and an altitude effect on $\delta^{18}O$ of -0.2 ‰ per 100 m elevation gain (Schotterer, 2010). The

430   corresponding δ^2H values were defined by assuming that they lie on the GMWL (i.e., $\delta^2H = 8$

431   x $\delta^2H + 10$; Schotterer et al., 2010), which is consistent with our stable water isotope analyses

432   (Fig. 3). Except for the upper model boundary, $\delta^{18}O$ and δ^2H values were initially set to

433   arbitrary values of -10 and -70 ‰, respectively (Table 1).

434   Since the model was defined as a single, fractured rock continuum, the uptake of Cl from

435   the proposed ancient porewater source (Seelig and Bucher, 2010; Wanner et al., 2017) to the

436   initially Cl free meteoric water was abstracted by specifying the kinetic release of Na and Cl

437   from a generic solid NaCl source ($NaCl_{(s)} = Na^+ + Cl^-$) with a fixed dissolution rate of 3 x 10$^-$

438   ^{14} mol kg_{H2O}^{-1} s^{-1} (0.03 mg kg_{H2O}^{-1} a^{-1}). This rate was numerically estimated by approximating

439   the Cl concentration profile observed along the Amsteg section (Fig. 2d). The calibrated rate

440   agrees well with fracture area normalized Cl uptake rates of 0.07–0.12 mg m^{-2} a^{-1} estimated

for groundwater circulating in the granitic basement in the region of Laxemar, Sweden (Waber et al., 2012). In Waber et al. (2012), the uptake of Cl from such porewater source was associated with a shift of $\delta^{18}O$ and δ^2H values away from the GMWL towards higher values, which was not observed for our samples (Fig. 3). Therefore, the uptake of water with significantly less negative $\delta^{18}O$ and δ^2H values than meteoric water from the proposed porewater source was neglected in our model.

4.4. Initial and boundary conditions

At the upper model boundary the temperature and pressure were prescribed to 1 bar and 4 °C, respectively. In doing so, we neglect the unsaturated zone and assume that the entire basement is fully saturated, which means that the water table is constrained by the topographic surface and that infiltration and exfiltration is allowed through the entire upper model boundary. Multiple studies have shown that this approximation is valid for the simulation of regional flow problems in orogenic crystalline settings (Tiedeman et al., 1998; Bossong et al., 2003; Caine et al., 2006; Taillefer et al., 2018). For our study, it is particularly justified by the lack of detailed information on the local water table and the rather large vertical model extent ($\leqslant 9$ km), for which the regional flow field is only weakly affected by the extent of the unsaturated zone. By allowing the flux of meteoric water through the upper model boundary during the entire course of our simulations, we assume (i) that the Hüfi-Glacier located <3200 m a.s.l. in the N–E part of the model domain (Fig. 1) represents a hydrological-active, warm-based glacier and (ii) that the meteoric water infiltration rate during past glaciation periods remained constant. While assumption (i) is justified given that in the Alps, evidence for hydraulically active, warm-based glaciers up to an altitude of 2600 m a.s.l. has been reported even during the last glacial maximum (18 ka ago) when the mean annual temperature was 12 ± 3 °C lower than today (Peyron et al., 1998; Wirsig et al., 2016), (ii) represent an important model simplification of which the implications will be discussed together with the model results.

468   Initially, a hydrostatic pressure distribution and a typical regional conductive geothermal

469   gradient of 25 °C km^{-1} (Vernon et al., 2008) were defined throughout the model domain (Fig.

470   7). The lateral and lower model boundaries were defined as no flux boundaries with respect to

471   fluid flow whereas the lateral boundaries were defined as no flux boundaries for heat

472   transport as well. The definition of the later model boundaries as no flux boundaries is

473   justified by the absence of heat sources other than the one responsible for the regional

474   geothermal gradient and because cross-catchment flow (i.e. across the horizontal boundaries)

475   is likely negligible. Across the lower model boundary, conductive heat transport was allowed

476   by fixing the temperature to 186 °C, which is consistent with the mean surface altitude of

477   1850 m a.s.l. within the model domain and a geothermal gradient of 25 °C km^{-1}.

478   The permeability of the fractured rock continuum (k) was defined as a function of

479   depth according to the relation derived from hydraulic tests performed in similar settings

480   worldwide (Stober and Bucher, 2007; Stober and Bucher, 2015),

481

482     $\log (k) = -1.38 \times \log(z) - 15.4$ (7)

483

484   where z refers to the depth (km) below the surface and k is the intrinsic vertical permeability

485   (m^2). Figure 6 shows that this relation is able to match the permeability recorded along the

486   nearby Sedrun section of the tunnel (Masset and Loew, 2013). To account for the steeply

487   dipping units (Fig. 2a) and nearly vertical fracture systems suggesting that flow is directed

488   vertically, a permeability anisotropy factor of 10 was considered between horizontal and

489   vertical direction with higher values associated with the orientation of factures. Consequently,

490   the specified permeability in x- and y- direction was 10 times lower than the one defined by

491   equation (7). In analogy to the permeability, the porosity was also specified as a function of

492   depth. In the absence of any information on the porosity-permeability relationship, our

493   simulations consider a linear fracture porosity decrease with depth (Fig. 6). The maximum

494   and minimum values (2.1 and 0.1 %) were taken from Hg porosity measurements performed

495   on gneisses and granites of a water conducting shear zone exposed in the nearby Grimsel Test

496   Site (Bossart and Mazurek, 1991).

497   Other physical and thermal properties (e.g. density, thermal conductivity) were

498   defined according to measurements performed in the nearby Grimsel Test Site (Keusen et al.,

499   1989; Kuhlmann and Gaus, 2014). All model parameter are listed in Table 1. Initial and

500   boundary conditions for simulating the fate of Cl and stable water isotopes were defined as

501   described above in detail, and the corresponding values are listed in Table 1.

502

503   **5. Model results and discussion**

504

505   **5.1. General flow system**

506   Selected results for the full model domain are shown in Figures 8 and 9. Computed

507   average linear vertical flow velocities (Fig. 8a) demonstrate that meteoric water infiltration

508   occurs at high altitude ($v_Z \leq 0$, lower limit of color scale), whereas upward directed flow

509   zones are found beneath major valleys such as the Maderaner Valley ($v_Z \geq 0$). The temporal

510   evolution of $\delta^{18}O$ values displays "plumes" of water with low $\delta^{18}O$ values originating from

511   the infiltration at high altitude (Fig. 9). These plumes may reach the lower model boundary (-

512   5.4 km a.s.l.) after a few 10 k years, and then migrate laterally before ascending towards the

513   surface of major valleys where they yield isotopically light values as well. Because our model

514   considers continuous uptake of Cl along flow paths, these regional circulation systems are

515   also expressed by the simulated Cl concentration distribution at chemical steady state (Fig.

516   8b), which is achieved after about 150 ka during the course of the simulation (Fig. 10).

517   Downward directed flow is indicated by the increase of Cl along the flow path towards

518   greater depth (Fig. 8b). In turn, upward directed flow below major valleys is manifested by

519   elevated Cl concentrations indicating maximum residence times.

520   Despite the infiltration of cold water at the surface (T = 4°C) and the upflow of heated

521   water from the lower model boundary (T = 186 °C), these flow zones only yield minor

522   temperature anomalies compared to the initially specified conductive temperature distribution

19

523   (Fig. 8 vs. Fig. 7). This is because flow velocities and hence water fluxes are rather small and

524   heat transport is dominated by conduction rather than by advection. Below the Maderaner

525   Valley for instance, the computed upflow velocity is about 2 m year^{-1}, whereas the model

526   predicts a downflow velocity below the Chrüzlistock of less than 0.5 m year^{-1} (Fig. 2f).

527

528   **5.2. Model results vs. geochemical constraints**

529   The comparison between parameter profiles observed along the Amsteg section of the

530   tunnel and the corresponding simulation results is given in Figure 2. Despite that the tunnel

531   was not explicitly considered in our model, the agreement is quite good. First, our model

532   predicts positive z-velocities and thus ascending water up to a distance of about 12.5 km

533   along the tunnel and negative z-velocities indicating downflow for the remainder of the

534   Amsteg section (Fig. 2f). These flow zones are consistent with the interpretation of the spatial

535   distribution of the silica phase saturation state (Fig. 2c), the Cl concentrations (Fig. 2d), and

536   the Cl vs. temperature correlation observed in groundwater exfiltrating into the tunnel (Fig.

537   4a), although the computed upflow zone extends up to 12.5 along the tunnel while Figure 4a

538   suggests that the first (i.e. ascending) group of groundwater samples extends up to 11.5 km

539   only. The maximum upflow velocity was computed for the segment where the tunnel

540   crosscuts the Bristen Granite beneath the Maderaner Valley (at ca. 9 km) (Fig. 2f). This is the

541   only segment along the tunnel where the collected groundwater was supersaturated with

542   respect to quartz and chalcedony (Fig. 2c) and hence indicates a comparatively fast ascending

543   fluid (Wanner et al., 2014). The simulated coupled thermal-hydraulic processes further yield a

544   temperature profile that matches the observed profile within reasonable uncertainty (Fig. 2e).

545   The total flux of ascending water computed for the entire Bristen Granite segment was 0.008

546   L s^{-1}, which is 850 times lower than the total discharge recorded along this particular segment

547   (6.97 L s^{-1}). Because the tunnel was not explicitly considered in our model, however, it is

548   challenging to directly compare computed flow rates to those measured in the tunnel. The

549   strong discrepancy is likely related to the facts that the construction of the tunnel induced a

550   strong pressure drop of likely more than 100 bar (Masset and Loew, 2013) and that with the

551 chosen model setup (e.g. discretization/resolution, not considering the tunnel), shallow

552 mixing with dilute meteoric water from the surface is not fully captured by the model.

553 Second, the model is capable of reconstructing the shape of the observed Cl

554 concentration profile (Fig. 2d), although it over- and underestimates the Cl concentration

555 along the Bristen Granite and the Intschi zone, respectively. In analogy to the flow rate

556 discrepancy, the overestimation of the Cl concentration along the Bristen Granite (at ca. 9

557 km) is due to the fact that shallow mixing with dilute meteoric water from the surface as

558 identified from the corresponding correlations (Fig. 5) is not fully captured with the chosen

559 model setup. In contrast, the underestimation along the Intschi zone (at ca. 10 km along the

560 tunnel) is likely due to a different chemical composition of the porewater in the differently

561 composed lithologies. Differences in the composition of the porewater serving as an

562 important Cl source is further suggested by the lack of correlations between groundwater

563 samples from the Bristen Granite and the Intschi zone (Fig. 5). The model is consistent with

564 such explanation in the sense that the computed origin of meteoric water discharging along

565 the Bristner Granite and the Intschi zone strongly differs. Computed streamlines (Fig. 11)

566 suggest that groundwater discharging along the Bristen Granite originates to the South-West

567 near the Bristen peak, whereas groundwater samples ascending beneath the Intschi zone

568 originate to the South-East in the vicinity of the Chrüzlistock.

569 Third, the simulated $\delta^{18}O$ values along the Amsteg section fall within the range

570 observed for groundwater samples (Fig. 2b), although simulations yield smaller $\delta^{18}O$

571 variations along the tunnel and a slightly lower mean $\delta^{18}O$ value (-14.6‰ vs. -13.9‰). This is

572 because (i) with the chosen model setup shallow mixing with dilute meteoric water from the

573 surface is not fully captured by the model, and (ii) the $\delta^{18}O$ and $\delta^{2}H$ values assigned to

574 infiltrating meteoric water were kept constant at the modern altitude dependent rainwater

575 values (Schotterer et al., 2010). Nevertheless, the fact that our model is able to approximate

576 the $\delta^{18}O$ profile observed at the tunnel level confirms that infiltration of meteoric water must

577 have mainly occurred at a period of time with climatic conditions similar to those of the

578 current Holocene interglacial period (<11.5 ka).

579

5.3. Timing of meteoric water infiltration

Along the tunnel, the mean residence times inferred from the simulated steady state Cl concentration profile and the specified constant Cl uptake rate of 3 x 10^{-14} mol kg_{H2O}^{-1} s^{-1} ($t_{average}$= [Cl]/Cl_{Uptake_rate}) range from 2,000 years below the Chrüzlistock to about 28,000 years beneath the Maderaner Valley (Fig. 2d). Since groundwater at the tunnel level represent mixtures of different flow paths, the actual travel time of a single water molecule or dissolved species can be much higher such as inferred from the Cl breakthrough curves computed for these two locations (Fig. 10). For the upward directed flow zone below the Maderaner Valley, the Cl breakthrough curve (Fig. 10b) demonstrates that it takes more than 100 k years of simulation time until meteoric water that has infiltrated near the Bristen peak reaches the tunnel level after having penetrated down to several kilometers below the tunnel (Fig. 11). In contrast, beneath the Chrüzlistock, computed Cl breakthrough curves (Fig. 10a) are consistent with the average residence times inferred from the Cl concentration profile (Fig. 2d), suggesting that meteoric water reaches the tunnel level after about 2,000 years. It should be noted, however, that these travel times represent rough estimations only. This is because they are proportional to the poorly constrained porosity and permeability distribution (Fig. 6) and because the infiltration rate of meteoric water was likely reduced during the last glaciation period and was certainly not constant over the past 100 ka such as assumed for our simulations. Nevertheless, since our model predicts travel times much less than 10 ka for groundwater samples collected along the postulated downward directed flow zone beneath the Chrüzlistock (Fig. 10a), it is evident that they must have infiltrated into the Aar Massif during the current Holocene interglacial period (<11.5 ka). In contrast, travel times much longer than 10 ka obtained for groundwater samples collected along the postulated upward directed flow zone below the Maderaner Valley (Fig. 10b) implies that these samples must have mostly infiltrated during similar but past climatic periods. Possible candidates are the Eemian (115– 130 ka) or the Meikirch interglacial (200–185 ka), of which the former is surprisingly consistent with the computed breakthrough curve.

607

6. Implication for the circulation of meteoric water in orogenic crystalline basements

Despite the comparatively simple nature of our model and the absence of any calibration work in addition to estimating the Cl uptake rate, the model is able to reasonably match all constraints identified from the chemical and isotopic composition of groundwater samples collected along the Amsteg section (Fig. 2). We consider this result as a strong quantitative confirmation that mountain topography operates as the most important driving force for meteoric water circulation in orogenic crystalline basements. Our simulations also confirm that in such settings, meteoric water can easily penetrate down to several kilometers deep into the brittle continental crust. For the simulated domain, the topographic driving force was large enough for meteoric water to penetrate down to a depth of 9 km below the surface where the estimated vertical permeability is less than 3×10^{-17} m^2 (Fig. 6). Since fluid flow in our model is conceptionalized to occur within a homogenously fractured rock characterized by a typical background permeability of granitic basement rocks (Stober and Bucher, 2007; Stober and Bucher, 2015), penetration down to several kilometers depth does not seem to be restricted by the presence of major fault zones with elevated permeability. Similarly, the topographic driving force was sufficient to push the infiltrated meteoric water horizontally before it ascends beneath major valleys, despite that the specified horizontal permeability was one order of magnitude lower than the vertical one ($<3\times10^{-18}$ m^2 at 9 km depth). This means that topography-driven flow can be sustained at a low horizontal permeability and does not necessary rely on regional fault zones.

In terms of practical applications, our simulations are in agreement with recent studies showing that in orogenic crystalline basements, thermal anomalies predominantly occur where major fault zones with permeabilities significantly above the background values considered in our model are exposed at valley floors (Taillefer et al., 2018, Wanner et al., 2019). This is because for such settings, the combination of hydraulic and structural driving forces is optimal. Thus, such settings represent ideal targets for the exploitation of orogenic geothermal systems such as proposed recently (Wanner et al., 2019). In the Central Alps,

23

635 promising examples are found within fault-hosted settings of the western part of the Aar

636 Massif at Brigerbad and of the Aiguilles Rouges Massif at Lavey-les-Bains (Sonney and

637 Vuataz, 2009; Valla et al., 2016). Both sites are located at the valley floor of the Rhone

638 Valley and they are characterized by thermal springs discharging at temperatures up to 65 °C

639 and are currently used as thermal spas. Moreover, Pastorelli et al. (2001) have shown that

640 thermal anomalies also occur in the Gotthard region such as in the nearby highway tunnel and

641 in an adjacent 500 m deep exploration borehole (28 °C in 450 m depth). Interestingly, these

642 anomalies are also found beneath a major valley, about 3 km south of the town of Andermatt.

643 Hence, they are fully consistent with our model results and further demonstrate that orogenic

644 geothermal systems are promising plays for geothermal power production.

645   Finally, our simulations confirm that circulation of meteoric water in orogenic crystalline

646 basements is slow and that significant infiltration of meteoric water may have occurred during

647 past interglacial periods dating more than 100 ka back in the past. This reinforces that

648 groundwater and/or porewater in crystalline basements may act as an archive for

649 palaeohydrologic variations (Waber et al., 2012). In terms of groundwater resources, the low

650 tunnel inflow rate computed for the most prominent upward directed flow zone beneath the

651 Maderaner Valley (0.008 L s^{-1}) suggest that deep circulation of meteoric water does not play a

652 major role on the regional water cycle, at least under the prevailing Alpine Climatic

653 conditions with atmospheric precipitation well above 1000 mm year^{-1} (MeteoSwiss, 2019).

654 However, for drier climatic conditions such as on the Tibet plateau with annual precipitation

655 rates below 500 mm year^{-1}, such rates might be significant for sustaining river baseflow and

656 spring discharge (Ge et al., 2008).

657

658 **7. Summary and conclusions**

659   Detailed knowledge about the circulation of meteoric water in non-magmatic,

660 orogenic belts is fundamental for assessing the potential of such settings for geothermal

661 power production (Wanner et al., 2019), as well as their use as potential groundwater

662   resources (Ge et al., 2008). To get more general insight into such regional hydrogeological

663   processes, and to particularly test the hypothesis that mountain topography operates as a first

664   order driving force for meteoric water circulation, we have conducted regional (20 x 10 x 9

665   km) thermal-hydraulic-chemical simulations of meteoric water circulation in the orogenic,

666   crystalline basement of the Aar Massif in the Central Alps, Switzerland. In the absence of

667   detailed hydraulic and structural data, the simulations were constrained by 122 chemical

668   analyses of groundwater samples collected during drilling of the World's longest and deepest

669   tunnel, the Gotthard railbase tunnel. Explicitly considering the surface topography in

670   combination with a previously published depth-dependent permeability distribution for

671   fractured crystalline rocks in our model was sufficient to reproduce key features of the

672   chemical analyses (e.g. salinity and temperature distribution), and up- and downward directed

673   flow zones inferred from geochemical constraints. To do so, the only parameter that had to be

674   calibrated in the model was the Cl uptake rate along the flow path. Performing additional

675   stable water isotope measurements and including their fate in the numerical simulations

676   allowed gaining further insights into the timing of meteoric water infiltration and subsequent

677   circulation. The main conclusions of this study are:

678   • Despite the lack of detailed structural and hydraulic data, 3D thermal-
679   hydraulic-chemical simulations constrained by geochemical data allowed
680   assessing regional and long-term topography-driven flow in orogenic
681   crystalline basements.

682   • Simulation results quantitatively confirm that the surface topography indeed
683   operates as a very strong driving force for meteoric water circulation in
684   orogenic crystalline basements. Owing to the induced hydraulic head gradient,
685   meteoric water infiltration occurs at high altitude whereas upward directed flow
686   zones (i.e. exfiltration) are found along major valleys.

687   • Down to 9 km depth, penetration of meteoric water is not limited by the
688   decrease in permeability typical of granitic basement rocks, suggesting that

689   advective fluid transport down to the brittle-ductile transition zone is likely

690   occurring in such systems. Without the occurrence of permeability anomalies

691   (i.e. major fault zones), however, the permeability and hence the flow rates are

692   too low for the formation of major thermal anomalies despite that in case of the

693   studied system meteoric water may attain temperatures well above 150 °C

694   during such deep infiltration.

695   • Based on the upward directed flow zones predicted along major valleys, our

696   simulations suggest that positive temperature anomalies do occur if fluid

697   upflow is promoted by the presence of major faults zones with elevated

698   permeability. Within the Aar and other crystalline alpine massifs, such

699   conditions are found frequently as manifested by the occurrence of multiple hot

700   springs currently used as thermal spas. Thus, we consider orogenic geothermal

701   systems as promising plays for geothermal power production.

702   • Due to the low permeability, circulation of meteoric water is slow (<2 m year^{-1})

703   and average groundwater residence times may strongly exceed the time period

704   of the current interglacial stage (>11.5 ka). This further underlines that

705   groundwater and/or porewater in orogenic crystalline basements may act as an

706   archive for palaeohydrologic variations during past interglacial periods.

707

713

References

Abrecht J. (1994) Geologic units of the Aarmassif and their pre-Alpine rock associations: a critical review. *Schweiz. Miner. Petrog.* **74**, 5-27.

Belgrano T. M., Herwegh M. and Berger A. (2016) Inherited structural controls on fault geometry, architecture and hydrothermal activity: an example from Grimsel Pass, Switzerland. *Swiss J. Geosci.* 109. 345-364.

Bossart P. and Mazurek M. (1991) Grimsel Test Site Structural Geology and water flow-paths in the migration shear zone. *Nagra Technical Report* **NTB 91-12**, 1-55.

Bossong C. R., Caine J. S., Stannard D. I., Flynn J. L., Stevens M. R. and Heiny-Dash J. S. (2003) Hydrologic conditions and assessment of water resources in the Turkey Creek Watershed, Jefferson County, Colorado, 1998–2001. *USGS Water-Resources Investigations Report* **03-4034**.

Bucher K., Zhang L. and Stober I. (2009) A hot spring in granite of the Western Tianshan, China. *Appl. Geochem.* **24**, 402-410.

Bucher K. and Stober I. (2010) Fluids in the upper continental crust. *Gefluids* **10**, 241-253.

Bucher K., Stober I. and Seelig U. (2012) Water deep inside the mountains: Unique water samples from the Gotthard rail base tunnel, Switzerland. *Chem. Geol.* **334**, 240-253.

Caine J. S., Manning A. H., Verplanck P. L., Bove D. J., Kahn K. G. and Ge S. (2006) Well construction information, lithologic logs, water level data, and overview of research in Handcart Gulch, Colorado: An alpine watershed affected by metalliferous hydrothermal alteration. *U.S. Geol. Surv. Open File* **06–1189**.

Cartwright I. and Buick I. S. (1999) The flow of surface-derived fluids through Alice Springs age middle-crustal ductile shear zones, Reynolds Range, central Australia. *J. Metamorph. Geol.* **17**, 397-414.

Choukroune P. and Gapais D. (1983) Strain pattern in the Aar Granite (Central Alps): Orthogneiss developed by bulk inhomogeneous flattening. *J. Struct. Geol.* **5**, 411-418.

Connolly J. A. D. and Podladchikov Y. Y. (2015) An analytical solution for solitary porosity waves: dynamic permeability and fluidization of nonlinear viscous and viscoplastic rock. *Geofluids* **15**, 269-292.

Craw D., Koons P. O., Zeitler P. K. and Kidd W. S. F. (2005) Fluid evolution and thermal structure in the rapidly exhuming gneiss complex of Namche Barwa–Gyala Peri, eastern Himalayan syntaxis. *J. Metamorph. Geol.* **23**, 829-845.

Croucher A. E. (2015) Recent developments in the PyTOUGH scripting library for TOUGH2 simulations. *Proceedings 37th New Zealand Geothermal Workshop. Taupo, New Zealand: The University of Auckland.*

Diamond L. W., Wanner C. and Waber H. N. (2018) Penetration depth of meteoric water in orogenic geothermal systems. *Geology* **46**, 1063-1066.

Dzikowski M., Josnin J. Y. and Roche N. (2016) Thermal Influence of an Alpine Deep Hydrothermal Fault on the Surrounding Rocks. *Groundwater* **54**, 55-65.

FOEN (2014) ISOT module of the NAQUA - National Groundwater monitoring program. *Swiss Federal Office For the Environment (FOEN)* https://http://www.bafu.admin.ch/bafu/en/home/topics/water/info-specialists/state-of-waterbodies/state-of-groundwater/naqua-national-groundwater-monitoring/isot-module.html accessed on 27.5.2019.

FOEN (2015) Einzugsgebietsgliederung Schweiz, EZGG: Topoggraphische Einzugsgebiete der Schweizer Gewässer. *Swiss Federal Office For the Environment (FOEN)* http://www.bafu.admin.ch/ezgg-ch accessed on 8.10.2019.

Forster C. and Smith L. (1988) Groundwater flow systems in mountainous terrain: 2. Controlling factors. *Water Resour. Res.* **24**, 1011-1023.

Ge S., Wu Q. B., Lu N., Jiang G. L. and Ball L. (2008) Groundwater in the Tibet Plateau, western China. *Geophys. Res. Lett.* **35**.

Goderniaux P., Davy P., Bresciani E., de Dreuzy J-R. and Le Borgne T. (2013) Partitioning a regional groundwater flow system into shallow local and deep regional flow compartments. *Water Res. Research*, **49**, 2274-2286.

Grasby S. E., Ferguson G., Brady A., Sharp C., Dunfield P. and McMechan M. (2016) Deep groundwater circulation and associated methane leakage in the northern Canadian Rocky Mountains. *Appl. Geochem.* **68**, 10-18.

Hofmann B. A., Helfer M., Diamond L. W., Villa I. M., Frei R. and Eikenberg J. (2004) Topography-driven hydrothermal breccia mineralization of Pliocene age at Grimsel Pass, Aar massif, Central Swiss Alps. *Schweiz. Miner. Petrog.* **84**, 271-302.

Hubbert M. K. (1940) The theory of groundwater motion. *The Journal of Geology* **48**, 785-944.

Hunziker J. C., Martinotti G. and Marini L. (1990) The waters of the Simplon tunnel (Swiss-Italian Alps) and of the adjacent Ossola district (Italy): geothermal considerations. *Geoth. Res. T.* **14-II**, 1477-1482.

Ingebritsen S. E. and Manning C. E. (1999) Geological implications of a permeability-depth curve for the continental crust. *Geology* **27**, 1107-1110.

International-Formulation-Committee (1967) *Formulation of the Thermodynamic Properties of Ordinary Water Substance*. IFC Secretariat, Düsseldorf, Germany.

Keusen H. R., Ganguin J., Schuler P. and Buleti M. (1989) Felslabor Grimsel: Geologie. *Nagra Technischer Bericht* **NTB 87-14**.

Kuhlmann U. and Gaus I. (2014) Inverse modelling of the FEBEX in situ test using iTOUGH2. *Nagra Arbeitsbericht* **NAB 14-20**, 1-33.

Labhart T. P. (1999) Aarmassiv, Gotthardmassiv und Tavetscher Zwischenmassiv: Aufbau und Entstehungsgeschichte, in: Loew, S., Wyss, R. (Eds.), Symposium Geologie Alptransit, Zürich. Balkema, Rotterdam, pp. 31-43.

Laws S., Eberhardt E., Loew S. and Descoeudres F. (2003) Geomechanical Properties of Shear Zones in the Eastern Aar Massif, Switzerland and their Implication on Tunnelling. *Rock Mech. Rock Eng.* **36**, 271-303.

Maréchal J. C., Perrochet P. and Tacher L. (1999) Long-term simulations of thermal and hydraulic characteristics in a mountain massif: The Mont Blanc case study, French and Italian Alps. *Hydrogeol. J.* **7**, 341-354.

Masset O. and Loew S. (2013) Quantitative hydraulic analysis of pre-drillings and inflows to the Gotthard Base Tunnel (Sedrun Lot, Switzerland). *Eng. Geol.* **164**, 50-66.

MeteoSwiss (2019) Climate diagrams and normals per station. *Swiss Federal Office of Meteorology and Climatology (MeteoSwiss)* https**:**//http://www.meteoswiss.admin.ch/home/climate/swiss-climate-in-detail/climate-normals/climate-diagrams-and-normals--per-station.html accessed on 27.5.2019.

Mullis J., Dubessy J., Poty B. and O'Neil J. (1994) Fluid regimes during late stages of a continental collision: Physical, chemical, and stable isotope measurements of fluid inclusions in fissure quartz from a geotraverse through the Central Alps, Switzerland. *Geochim. Cosmochim. Acta* **58**, 2239-2267.

Nordstrom D. K., Ball J. W., Donahoe R. J. and Whittemore D. (1989) Groundwater chemistry and water–rock interactions at Stripa. *Geochim. Cosmochim. Acta* **53**, 1727-1740.

Pastorelli S., Marini L. and Hunziker J. (2001) Chemistry, isotope values (δD, $\delta^{18}O$, $\delta^{34}S_{SO4}$) and temperatures of the water inflows in two Gotthard tunnels, Swiss Alps. *Appl. Geochem.* **16**, 633-649.

Pearson F. J., Balderer W., Loosli H. H., Lehmann B. E., Matter A., Peters T., Schmassmann H., and Gautschi A. (1991): Applied Isotope Hydrogeology – A case study in Northern Switzerland. Studies in Environmental Science 43, Elsevier, Amsterdam, 481 pp.

Peyron O., Guiot J., Cheddadi R., Tarasov P., Reille M., de Beaulieu J.-L., Bottema S. and Andrieu V. (1998) Climatic Reconstruction in Europe for 18,000 YR B.P. from Pollen Data. *Quaternary Res.* **49**, 183-196.

Pfeifer H. R., Sanchez A. and Degueldre C. (1992) Thermal springs in granitic rocks from the Grimsel Pass (Swiss Alps): The late stage of a hydrothermal system related to Alpine Orogeny, in: Kharaka, Y.K., Maest, A.S. (Eds.), Proceedings of Water-Rock

824   Interaction WRI–7,. A.A. Balkema, Rotterdam, The Netherlands, Park City, Utah, pp.
825   1327-1330.
826 Preusser F., Graf H. R., Keller O., Krayss E. and Schlüchter C. (2011) Quaternary glaciation
827   history of northern Switzerland. *E&G Quaternary Sci. J.* **60**, 282-305.
828 Reed M. and Palandri J. L. (2006) SOLTHERM.H06, a database of equilibrium constants for
829   minerals and aqueous species. Available from the authors, University of Oregon,
830   Eugene, USA.
831 Reyes A. G., Christenson B. W. and Faure K. (2010) Sources of solutes and heat in low-
832   enthalpy mineral waters and their relation to tectonic setting, New Zealand. *J.*
833   *Volcanol. Geoth. Res.* **192**, 117-141.
834 Schaltegger U. (1994) Unravelling the pre-Mesozoic history of the Aar and Gotthard massifs
835   (Central Alps) by isotopic dating — a review. *Schweiz. Miner. Petrog.* **74**, 41-51.
836 Schneeberger R., Kober F., Lanyon B. G. W., Mäder U., Spillmann T. and Blechschmidt I.
837   (2019) Grimsel Test Site: Revisiting the site-specific geoscientific knowledge *Nagra*
838   *Technischer Bericht* **NTB 19-01**.
839 Schotterer U., Schürch M., Rickli R. and Stichler W. (2010). Wasserisotope in der Schweiz -
840   Neue Ergebnisse und Erfahrungen aus dem nationalen Messnetz ISOT. *Gas-Wasser-*
841   *Abwasser (GWA)* **12**, 1073-1081.
842 Seelig U. and Bucher K. (2010) Halogens in water from the crystalline basement of the
843   Gotthard rail base tunnel (central Alps). *Geochim. Cosmochim. Acta* **74**, 2581-2595.
844 Singleton M. J., Sonnenthal E. L., Conrad M. E., DePaolo D. J. and Gee G. W. (2005)
845   Multiphase reactive transport modeling of seasonal infiltration events and stable
846   isotope fractionation in unsaturated zone pore water and vapor at the Hanford site.
847   *Vadose Zone J.* **3**, 775-785.
848 Sonney R. and Vuataz F.-D. (2008) Properties of geothermal fluids in Switzerland: A new
849   interactive database. *Geothermics* **37**, 496-509.
850 Sonney R. and Vuataz F.-D. (2009) Numerical modelling of Alpine deep flow systems: a
851   management and prediction tool for an exploited geothermal reservoir (Lavey-les-
852   Bains, Switzerland). *Hydrogeol. J.* **17**, 601-616.
853 Steck A. and Hunziker J. (1994) The Tertiary structural and thermal evolution of the Central
854   Alps—compressional and extensional structures in an orogenic belt. *Tectonophysics*
855   **238**, 229-254.
856 Stober I., Richter A., Brost E. and Bucher K. (1999) The Ohlsbach Plume – Discharge of
857   deep saline water from the crystalline basement of the Black Forest, Germany.
858   *Hydrogeol. J.* **7**, 273-283.
859 Stober I. and Bucher K. (2007) Hydraulic properties of the crystalline basement. *Hydrogeol.*
860   *J.* **15**, 213-224.
861 Stober I. and Bucher K. (2015) Hydraulic conductivity of fractured upper crust: insights from
862   hydraulic tests in boreholes and fluid-rock interaction in crystalline basement rocks.
863   *Geofluids* **15**, 161-178.
864 Stober I., Zhong J., Zhang L. and Bucher K. (2016) Deep hydrothermal fluid–rock
865   interaction: the thermal springs of Da Qaidam, China. *Geofluids* **16**, 711-728.
866 Taillefer A., Guillou-Frottier L., Soliva R., Magri F., Lopez S., Courrioux G., Millot R.,
867   Ladouche B. and Le Goff E. (2018) Topographic and Faults Control of Hydrothermal
868   Circulation Along Dormant Faults in an Orogen. *Geochem. Geophy. Geosy.* **19**, 4972-
869   4995.
870 Thiebaud E., Gallino S. p., Dzikowski M. and Gasquet D. (2010) The influence of glaciations
871   on the dynamics of mountain hydrothermal systems: numerical modeling of the La
872   Léchère system (Savoie, France). *B. Soc. Géol. Fr.* **181**, 295-304.
873 Tiedeman C. R., Goode D. J. and Hsieh P. A. (1998) Characterizing a Ground Water Basin in
874   a New England Mountain and Valley Terrain. *Groundwater* **36**, 611-620.
875 Valla P. G., Rahn M., Shuster D. L. and van der Beek P. A. (2016) Multi-phase late-Neogene
876   exhumation history of the Aar massif, Swiss central Alps. *Terra Nova* **28**, 383-393.

877   van Geldern R. and Barth J. A. C. (2012) Optimization of instrument setup and post-run
878   corrections for oxygen and hydrogen stable isotope measurements of water by isotope
879   ratio infrared spectroscopy (IRIS). *Limnol. Oceanogr-Meth.* **10**, 1024-1036.
880   Vernon A. J., van der Beek P. A., Sinclair H. D. and Rahn M. K. (2008) Increase in late
881   Neogene denudation of the European Alps confirmed by analysis of a fission-track
882   thermochronology database. *Earth Planet. Sci. Lett.* **270**, 316-329.
883   Waber H. N., Gimmi T. and Smellie J. A. T. (2012) Reconstruction of palaeoinfiltration
884   during the Holocene using porewater data (Laxemar, Sweden). *Geochim. Cosmochim.*
885   *Acta* **94**, 109-127.
886   Waber H. N., Schneeberger R., Mäder U. K. and Wanner C. (2017) Constraints on evolution
887   and residence time of geothermal water in granitic rocks at Grimsel (Switzerland).
888   *Proced. Earth Plan. Sc.* **17**, 774-777.
889   Wanner C., Peiffer L., Sonnenthal E., Spycher N., Iovenitti J. and Kennedy B. M. (2014)
890   Reactive transport modeling of the Dixie Valley geothermal area: Insights on flow
891   and geothermometry. *Geothermics* **51**, 130-141.
892   Wanner C., Bucher K., Pogge von Strandmann P. A. E., Waber H. N. and Pettke T. (2017) On
893   the use of Li isotopes as a proxy for water–rock interaction in fractured crystalline
894   rocks: A case study from the Gotthard rail base tunnel. *Geochim. Cosmochim. Acta*
895   **198**, 396-418.
896   Wanner C., Diamond L. W. and Alt-Epping P. (2019) Quantification of 3D thermal anomalies
897   from surface observations of an orogenic geothermal system (Grimsel Pass, Swiss
898   Alps). J. *Gephys. Res.-Sol. Ea.* in press. Doi: 10.1029/2019JB018335.
899   Wickham S. M., Peters M. T., Fricke H. C. and O'Neil J. R. (1993) Identification of magmatic
900   and meteoric fluid sources and upward- and downward-moving infiltration fronts in a
901   metamorphic core complex. *Geology* **21**, 81-84.
902   Wintsch R. P., Christoffersen R. and Kronenberg A. K. (1995) Fluid-rock reaction weakening
903   of fault zones. *J Geophys Res* **100**, 13021–13032.
904   Wirsig C., Zasadni J., Ivy-Ochs S., Christl M., Kober F. and Schlüchter C. (2016) A
905   deglaciation model of the Oberhasli, Switzerland. *J. Quaternary Sci.* **31**, 46-59.
906   Xu T., Sonnenthal E. L., Spycher N. and Zheng L. (2014) TOUGHREACT V3.0-OMP
907   Reference Manual: A Parallel Simulation Program for Non-Isothermal Multiphase
908   Geochemical Reactive Transport. *LBNL Manual*
909   http://eesatough.lbl.gov/licensing/toughreact.html.
910
911

Table 1:Values and sources of parameters used in the numerical simulations

Parameter	Value	Meaning/source
Dimension of model		
N-S and E-W	10 x 20 km	Extent of Maderaner-Valley catchment
Base of model	-5400 m a.s.l.	6 km below tunnel, allows simulating fluid flow below tunnel
Upper boundary	Surface topography	Digital elevation model
Hydraulic properties		
Permeabililty (k) (except lower model boundary)	log k (m^2) = -1.38 x log(z) - 15.4	Stober and Bucher (2007); Bucher and Stober (2015)
Permeability at lower boundary	10^{-34} m^2	Infinitely low to define a no flux boundary for fluid flow
Porosity (ϕ)	Linear decrease from 2.1 to 0.1	Maximum and minimum values measured in nearby Grimsel Test Site (Bossart and Mazurek, 1991). A linear behavior because no porosity-permeability relation is available for the studied site.
Fixed pressure at surface (P_{surf})	1 bar	Atmospheric pressure
Fixed pressure at lower boundary (P_{low_bound})	685 – 718 bar	Hydrostatic pressure distribution assuming fully saturated conditions
Thermal properties		
Background surface temperature (T_{surf})	4 °C	Annual mean at average altitude (1850 m a.s.l.)
Geothermal gradient	25 °C km^{-1}	Vernon (2008)
Thermal conductivity of wet granite (λ)	3.34 W m^{-1} K^{-1}	Measurements in nearby Grimsel Test Site (Kuhleman and Gauss, 2014)
Fixed T at base of model	186 °C	Allows considering a heat flux across the lower model boundary corresponding to a geothermal gradient of 25 °C km^{-1}. T=186 °C results from the depth of the lower boundary (-5400 m a.s.l.) and the average surface altitude (1850 m a.s.l.)
Specific heat (c_p)	920 J kg^{-1} K$^-$1	Result of inverse modeling of in-situ experiment in nearby Grimsel test site (Kuhlmann & Gaus, 2014)
Rock density (ρ)	2690 kg m^{-3}	Measurements in nearby Grimsel Test Site (Keusen et al., 1989)
Chemical parameters		
Fixed δ^{18}O at upper model boundary	Altitude dependent (-10.9‰ at 800 m a.s.l;. -15.9 ‰ at 3300 m a.s.l.)	Schotterer et al. (2010)
Fixed δ^2H at upper model boundary	Altitude dependent (-77.1 ‰ at 800 m a.s.l;. -117.1 ‰ at 3300 m a.s.l.)	Schotterer et al. (2010)
Initial δ^{18}O and δ^2H	-10 and -70 ‰	Arbitrary, outside of measured range
Initial Cl conc.	1e-10 mol kg$_{H2O}^{-1}$	Meteoric water assumed to be Cl free
Constant NaCl$_{(s)}$ dissolution rate	3 x 10^{-14} mol kg$_{H2O}^{-1}$ s^{-1}.	Calibrated to match max. Cl conc. observed in tunnel inflows along Amsteg section

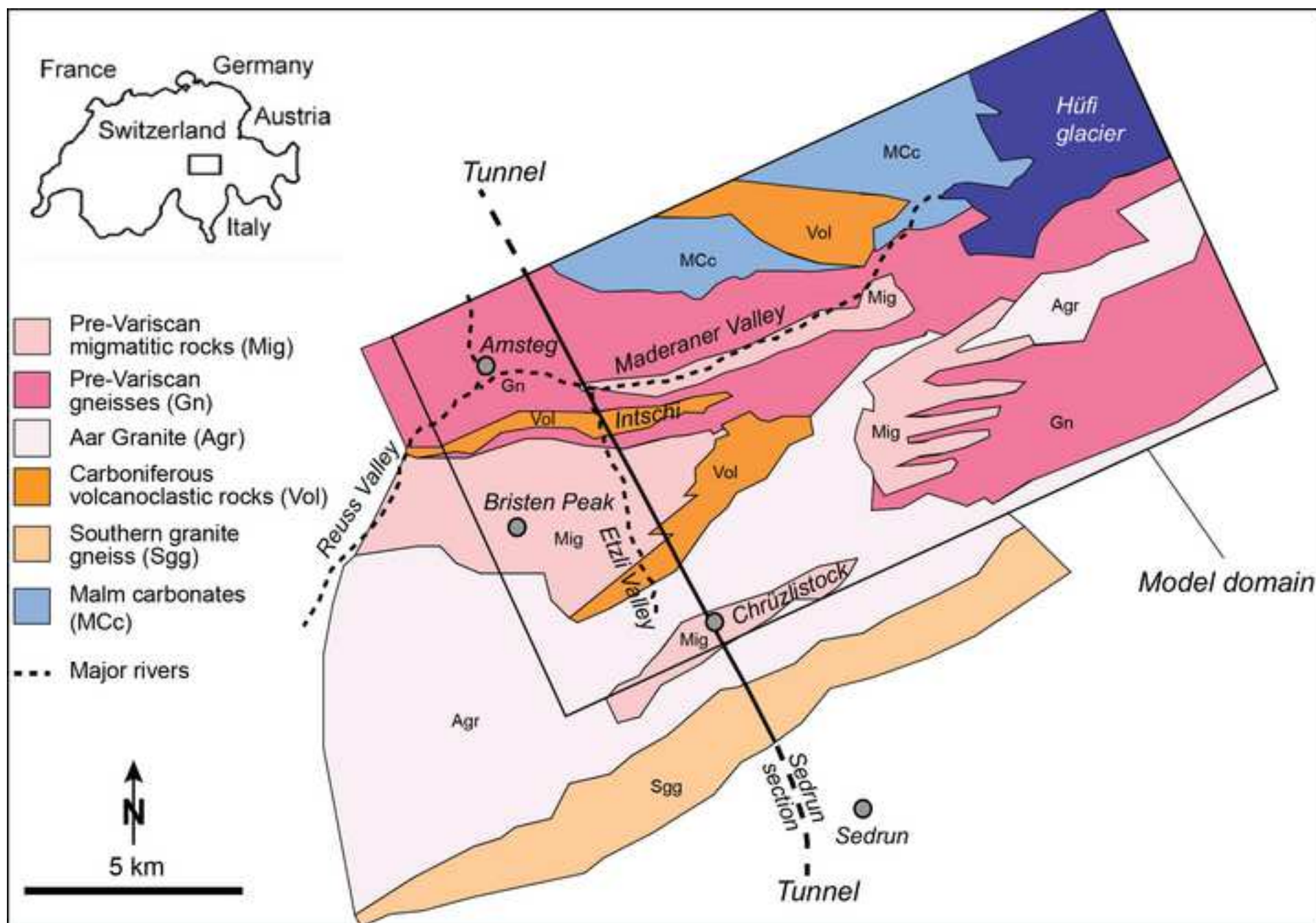**Figure 1**
Click here to download high resolution image
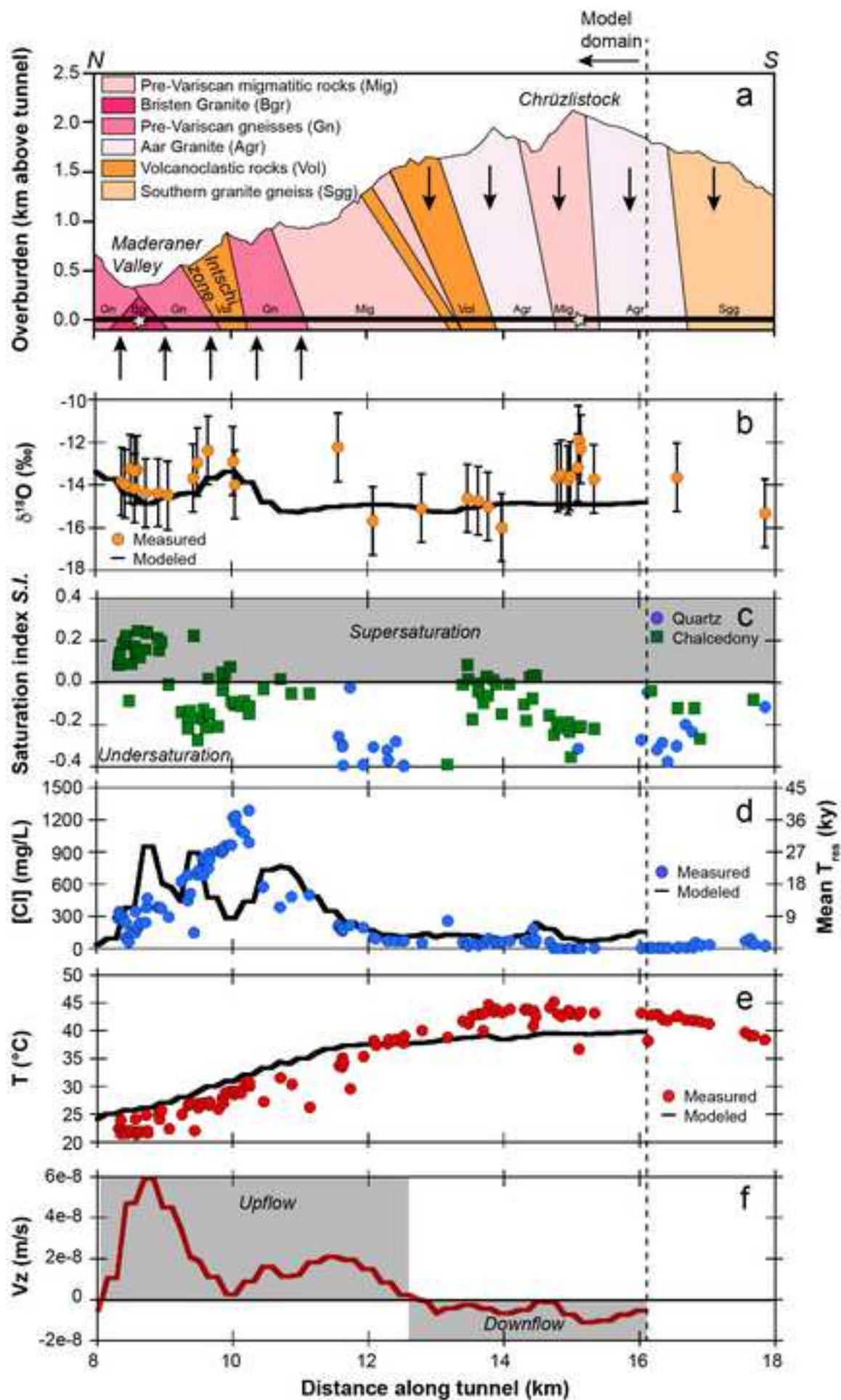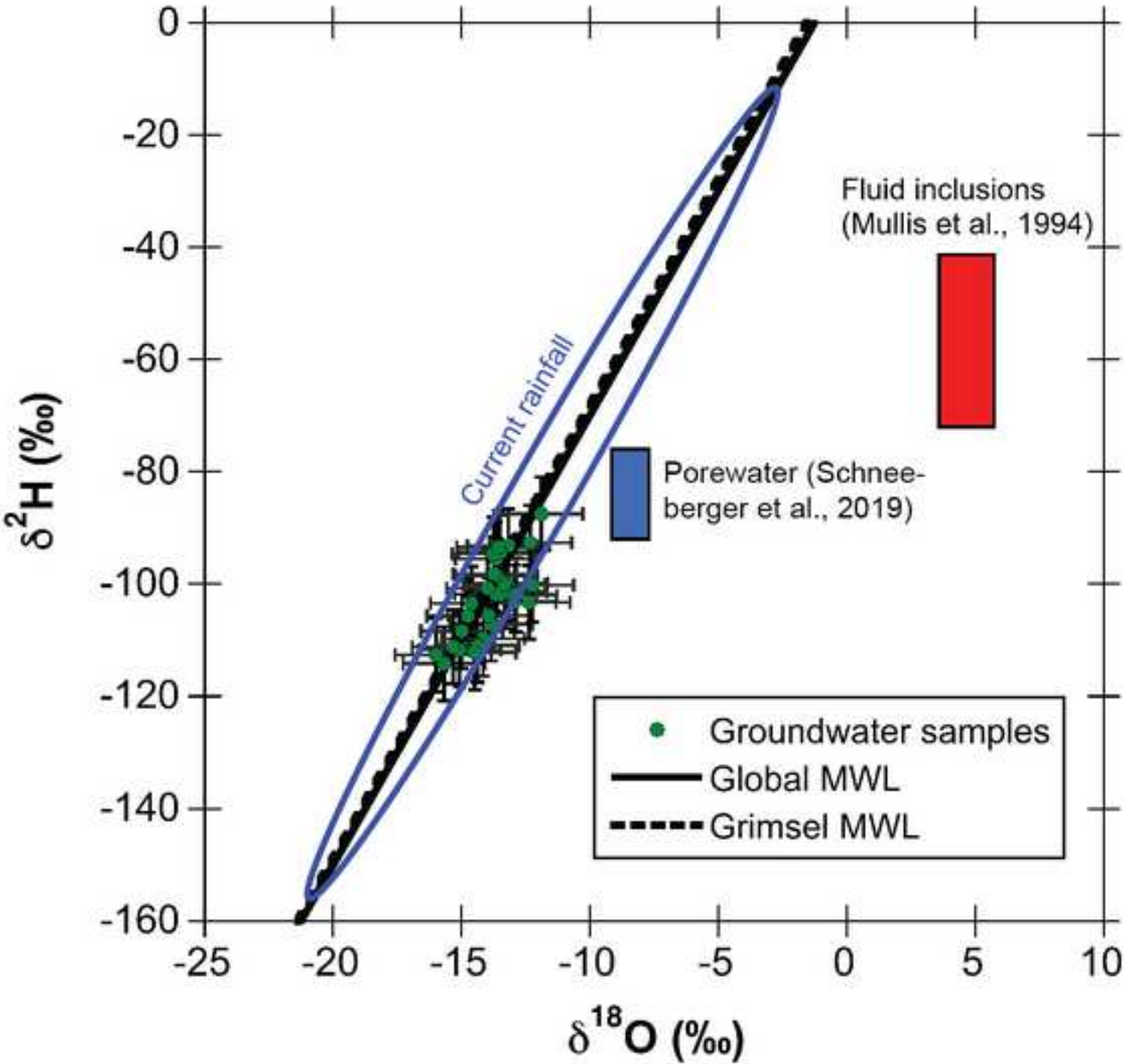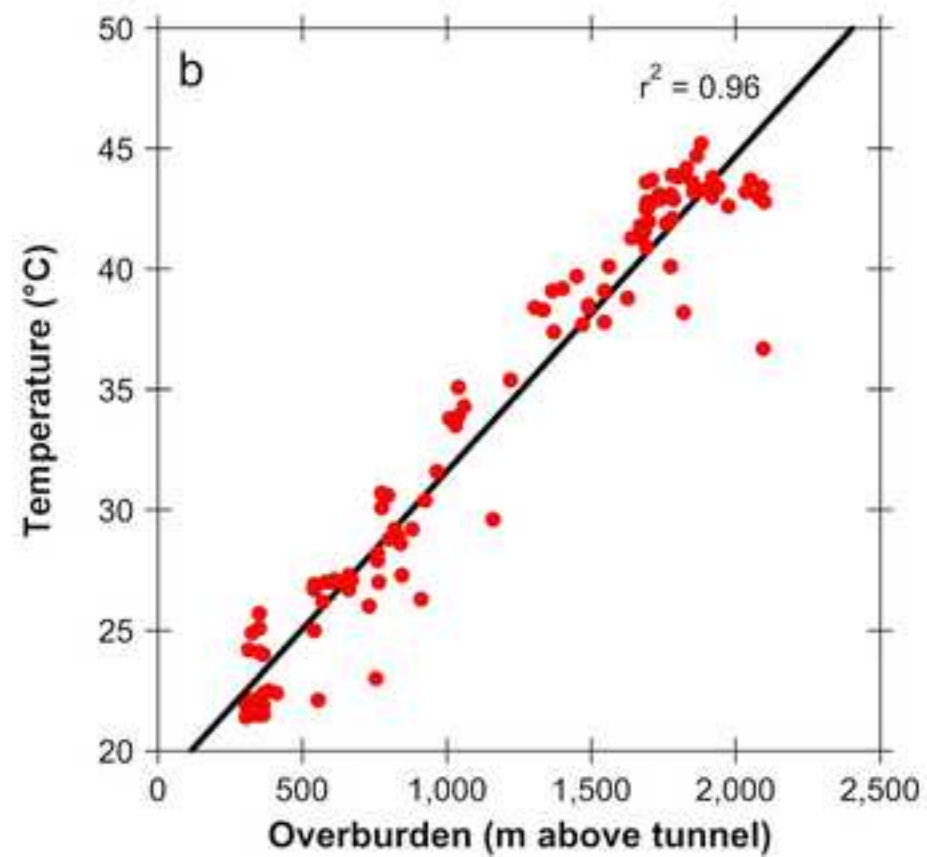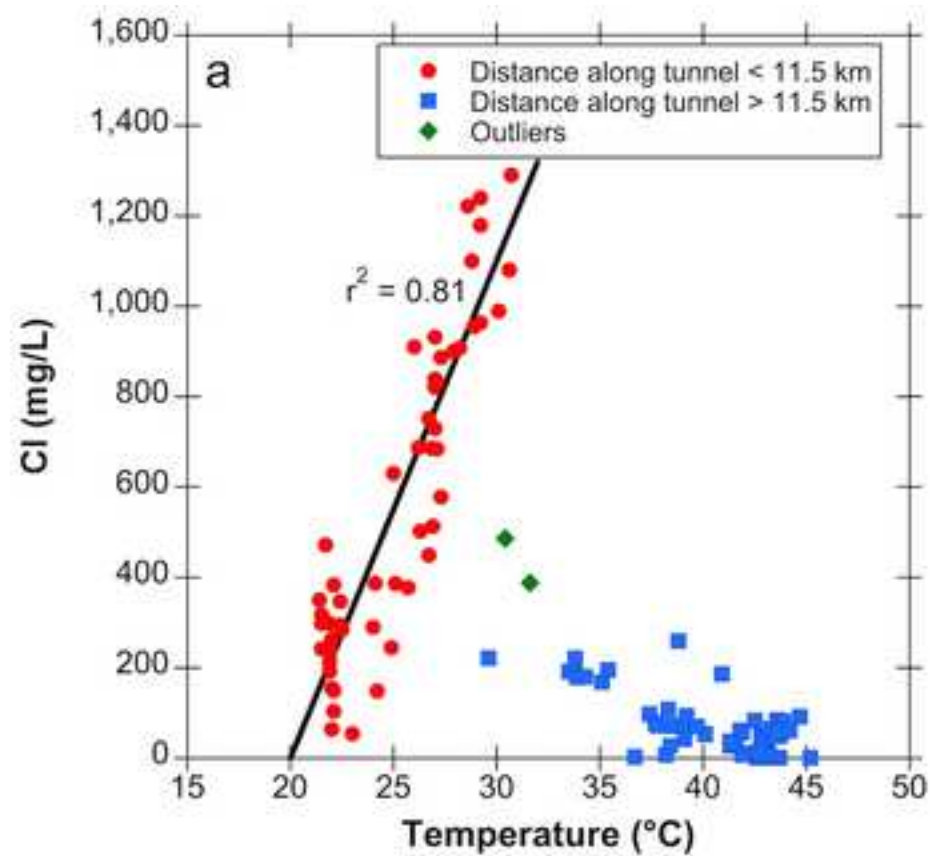
Figure 1
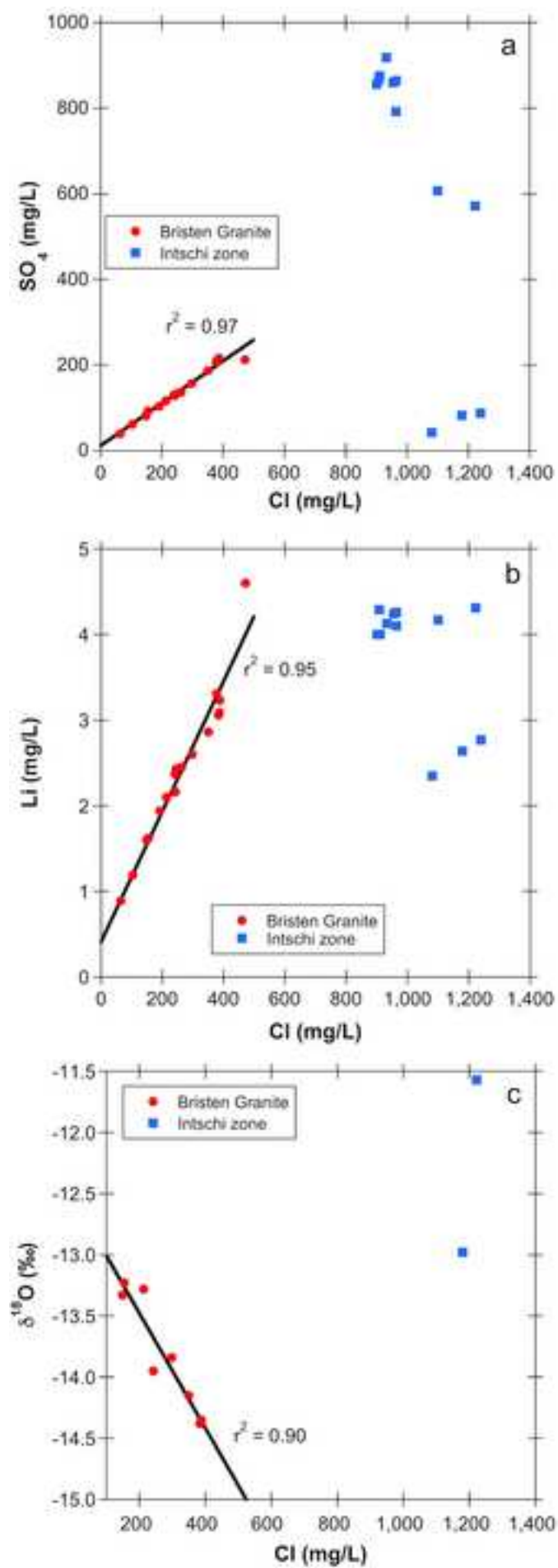
Figure 3

Figure 4

Figure 6
Click here to download high resolution image
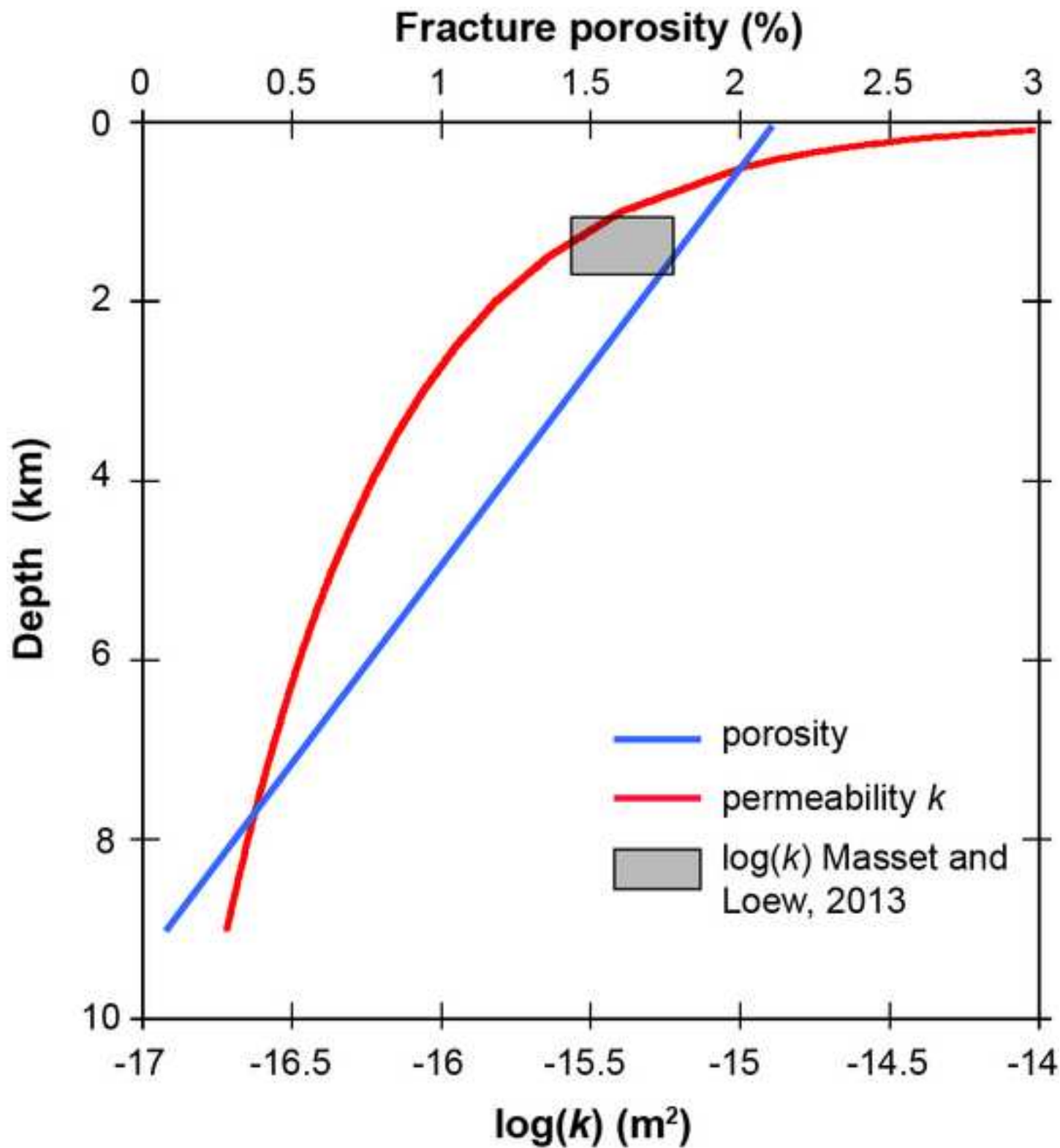
Figure 7
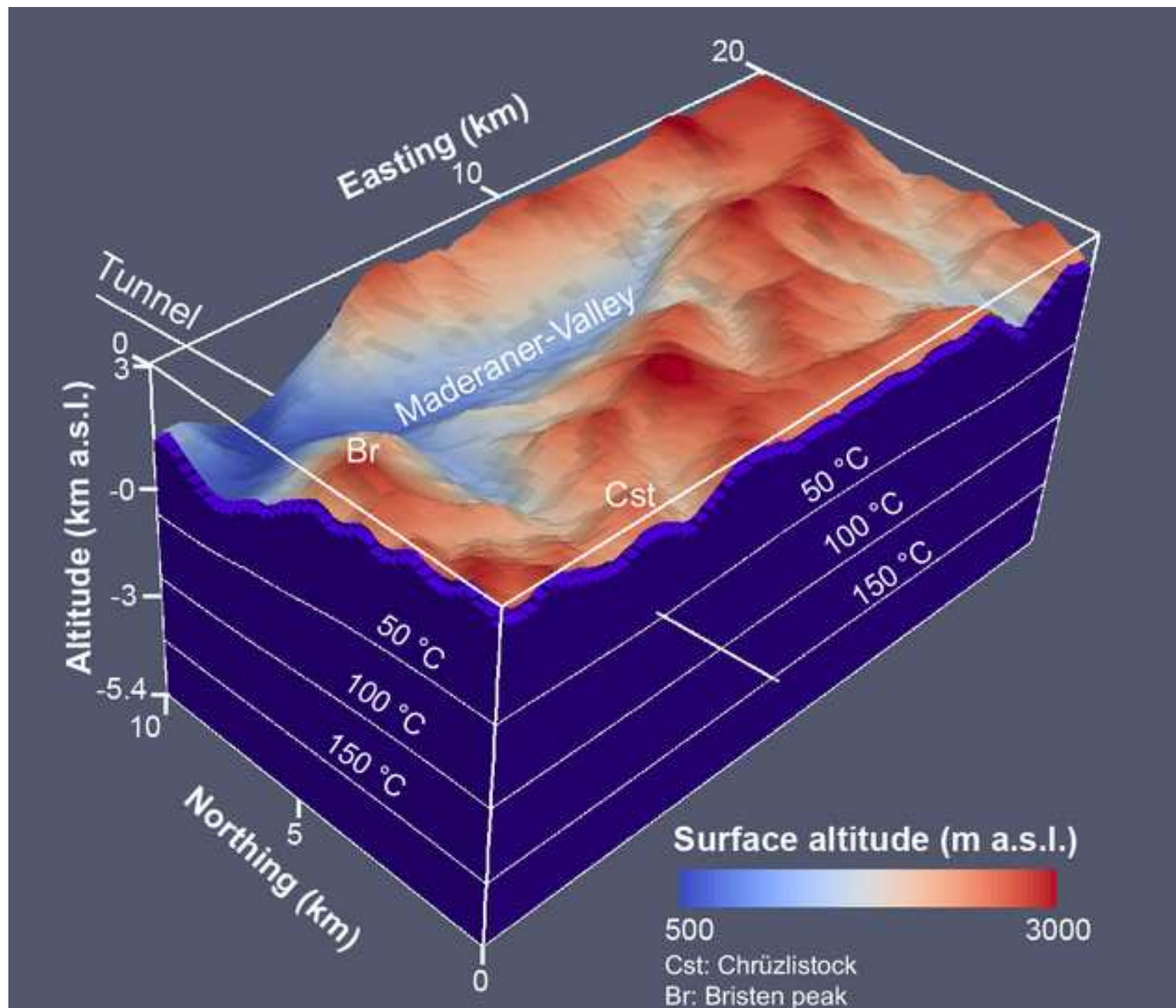
Figure 8
Click here to download high resolution image

a) after 5,000 years
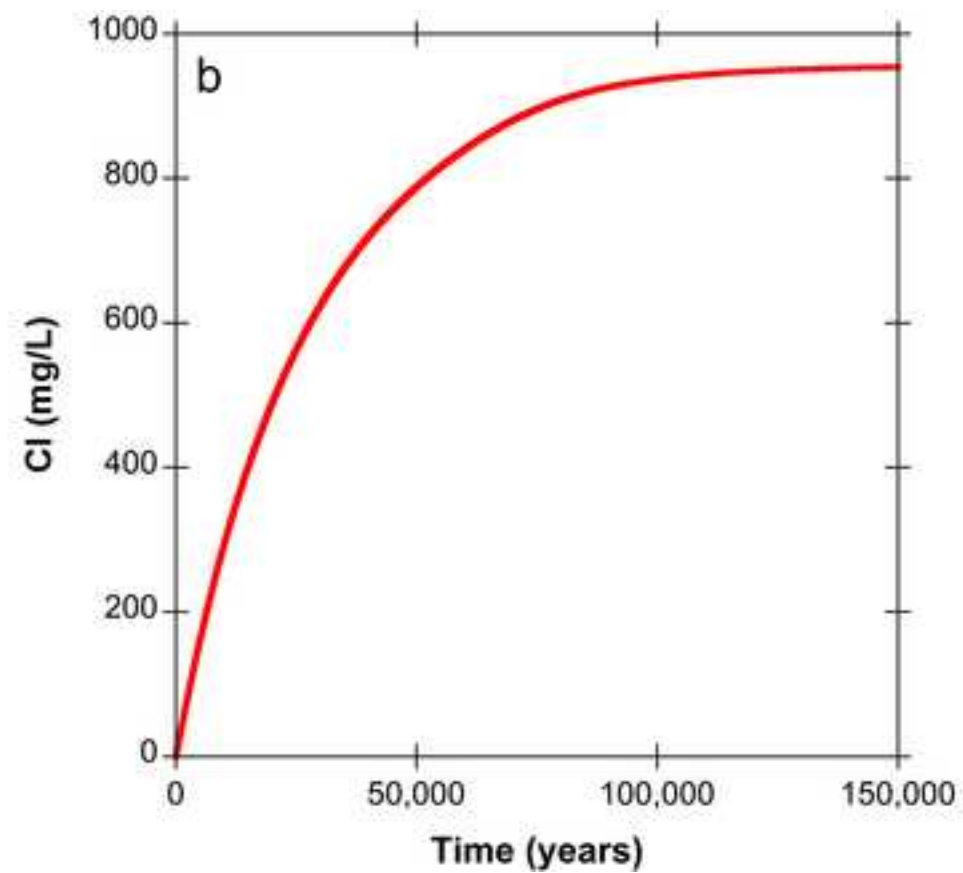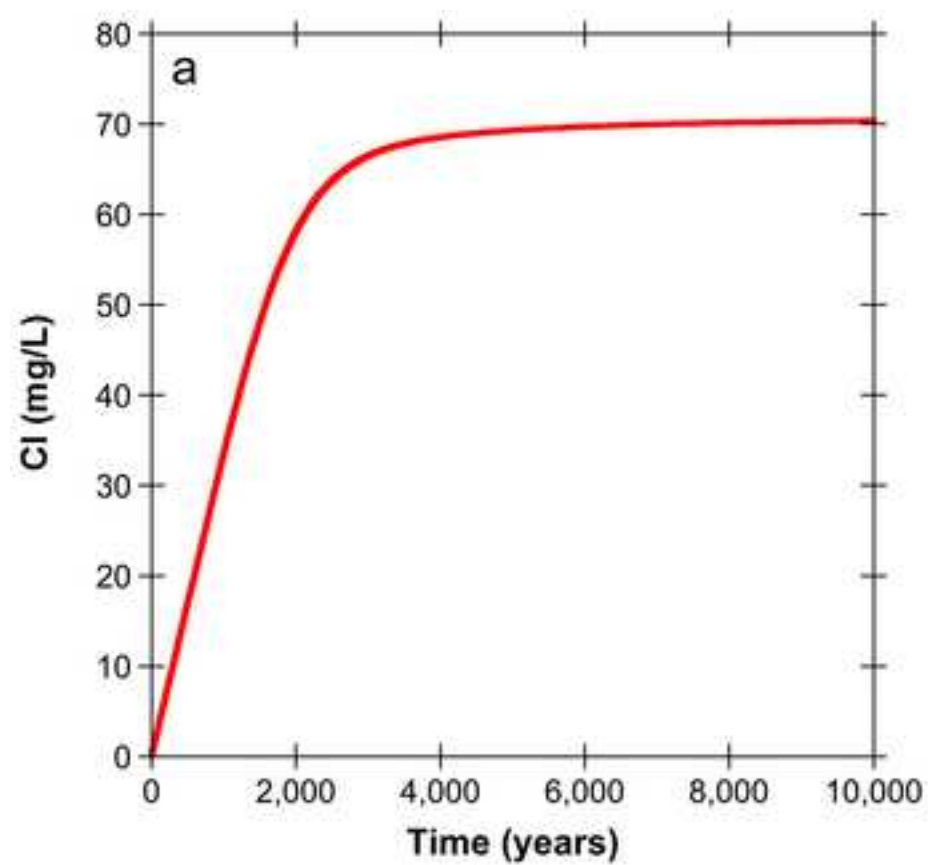
b) after 20,000 years

c) after 100,000 years
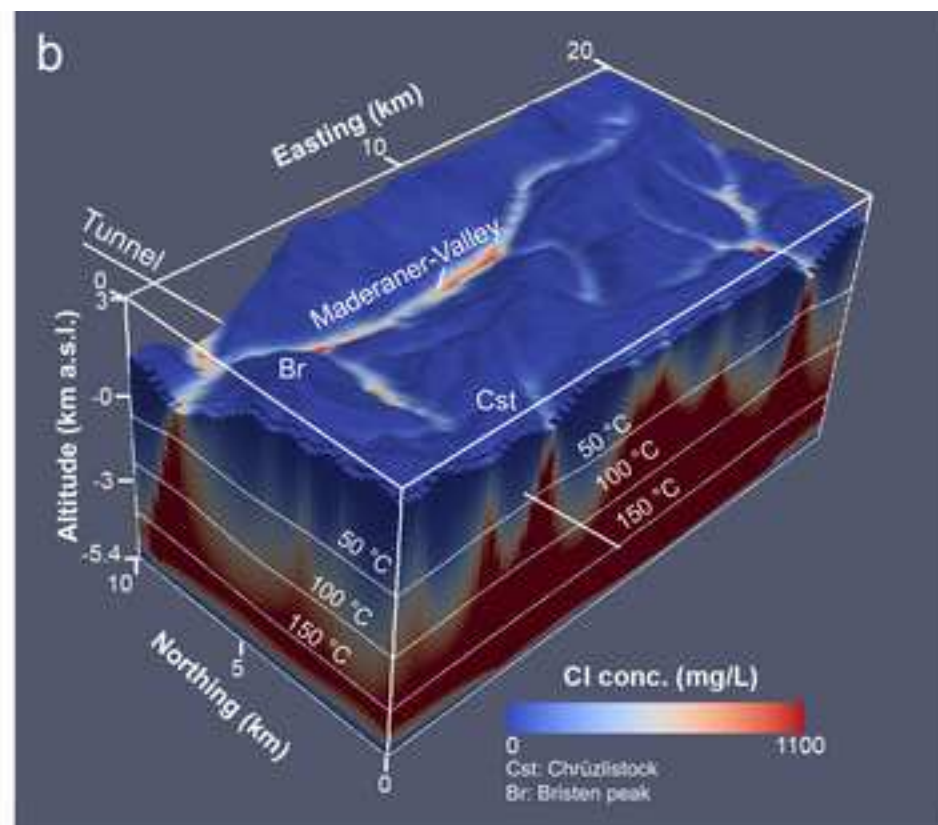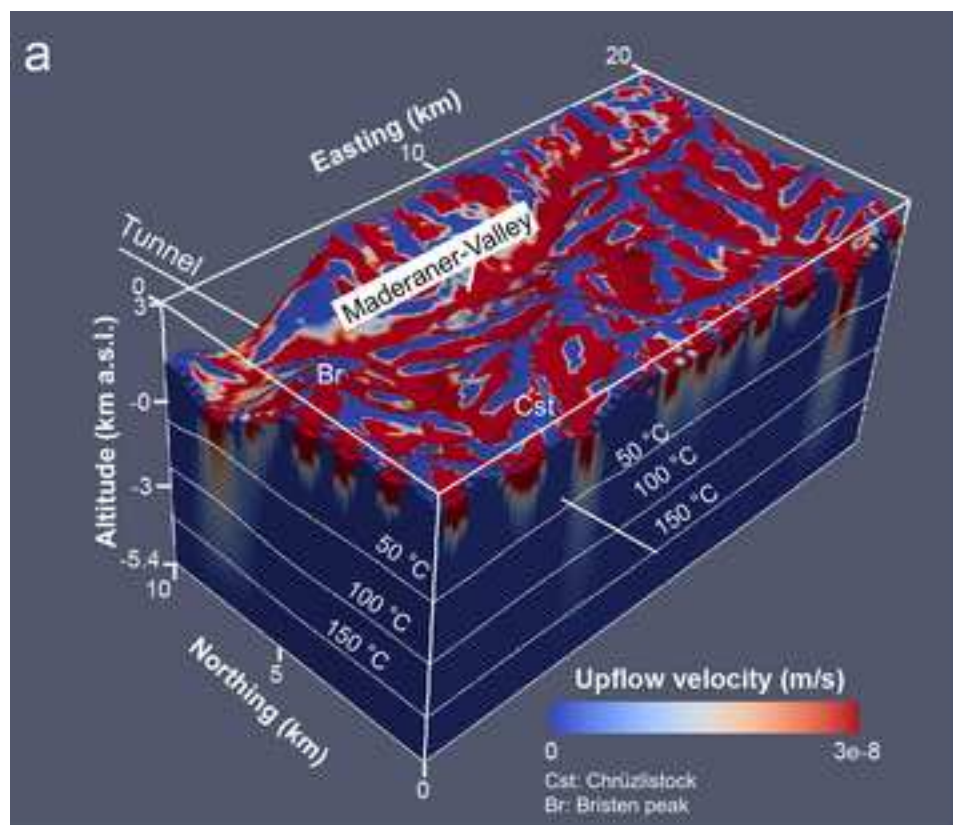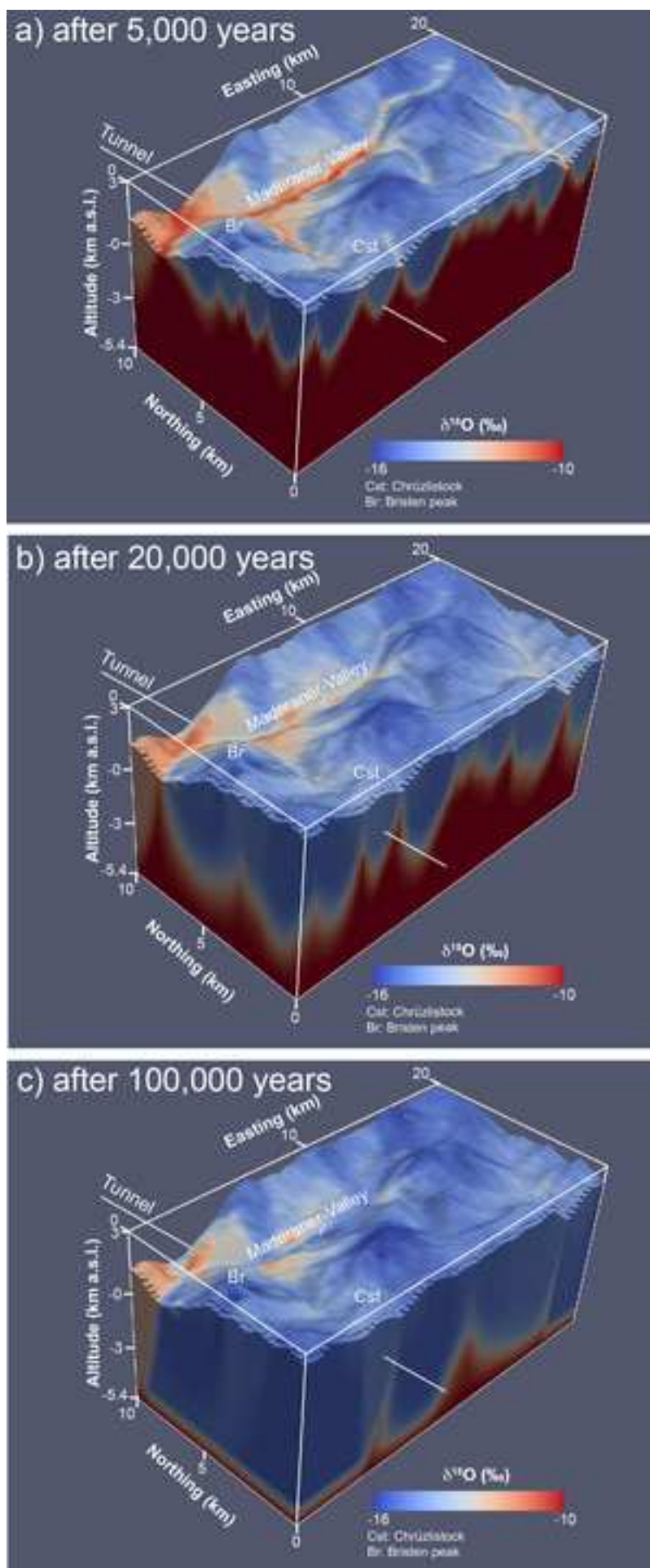
Figure 10
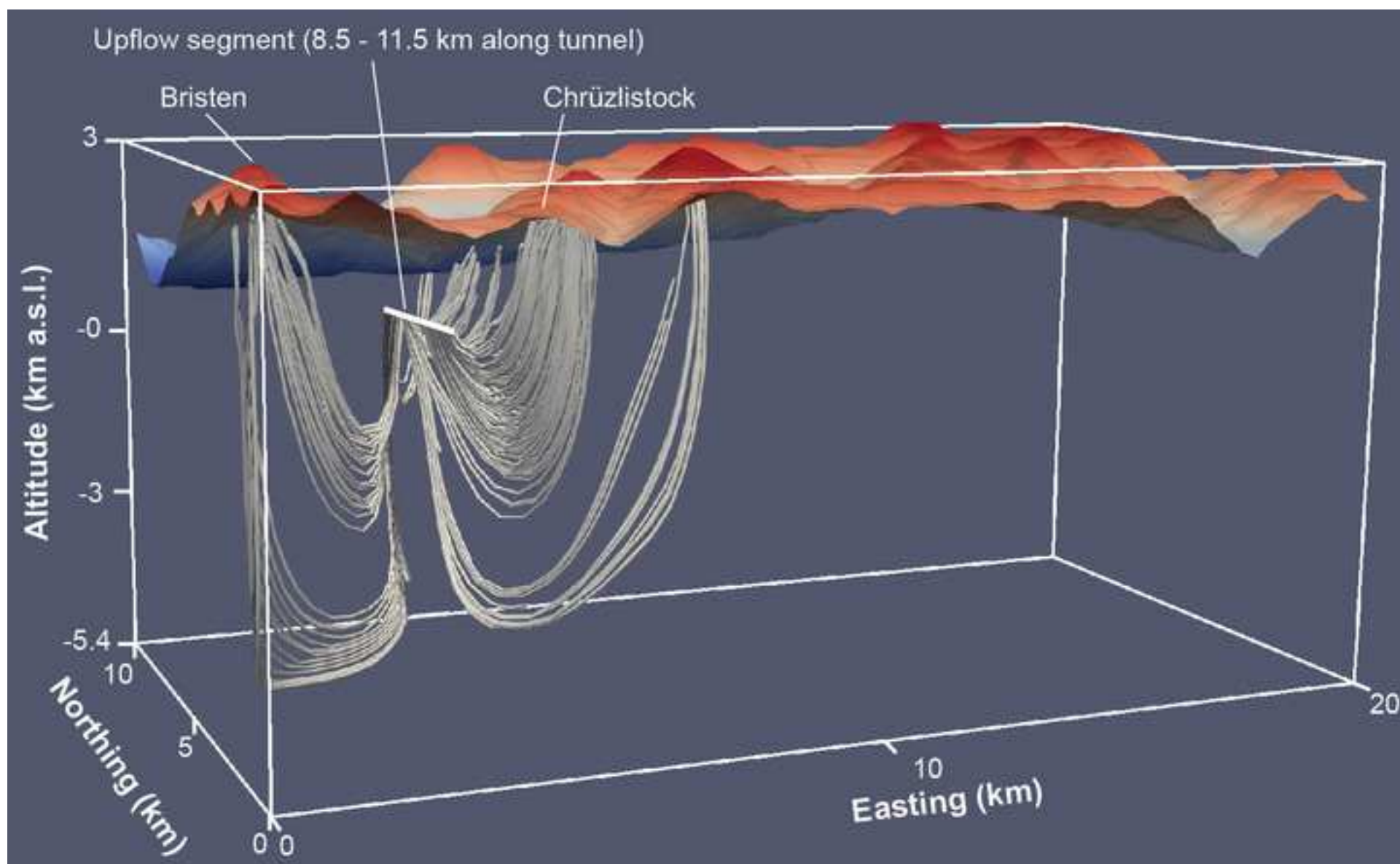**Click here to download high resolution image**

Figure Captions

Figure 1. Geological map of the eastern part of the Aar Massif (modified after Abrecht, 1994). The solid segment of the tunnel refers to the Amsteg section, for which numerous groundwater samples were collected and chemically analyzed (Bucher et al. 2012). The black rectangular illustrated the horizontal extent of the model domain.

Figure 2. Profiles through the Amsteg section of the Tunnel. (a) Geological units and downward and upward directed flow zones inferred form geochemical constraints. Star symbols denote locations, for which breakthrough curves are shown in Figure 10 (modified from Bucher et al., 2012). (b) Saturation indices of quartz (*pH*>9.5) and chalcedony (*pH*<9.5) in groundwater samples. (c) Measured and computed Cl concentrations of groundwater samples, as well as corresponding average residence times inferred from the computed Cl concentrations. (d) Measured and computed temperatures of groundwater samples. (e) Measured and computed $\delta^{18}O$ values of groundwater samples. (f) Z-component of the computed flow vectors, suggesting that downflow ($v_Z<0$ m s^{-1}) occurs at high altitude while a upwards directed flow zone ($v_Z>0$ m s^{-1}) exists beneath the Maderaner Valley at distances less than 12.5 km along the tunnel.

Figure 3. Stable O-H isotope signatures of 30 groundwater samples collected along the Amsteg section of the tunnel, all showing close association with meteoric water lines (MWL), as well as with current rainfall at the nearby Grimsel and Guttannen meteorological station (FOEN, 2014). Rectangles denote isotope signatures of porewater samples collected in similar geological units of the Aar Massif in the nearby Grimsel Test Site (Schneeberger et al., 2019), as well as in fluid inclusions of fissure quartz collected from different granitic units in the Aar Massif and representing ancient metamorphic fluids (Mullis et al., 1994). Error bars denote combined analytical and numerical (eq. (1)) errors.

Figure 4. Correlations observed for groundwater samples collected along the Amsteg section of the tunnel. (a) Linear correlation between Cl concentrations and the discharge temperatures observed for samples collected at a distance of less than 11.5 km along the tunnel. (b) Linear correlation between temperature and overburden, demonstrating that the regional geotherm of 25 °C km^{-1} (Vernon et al., 2008) controls the discharge temperature and that thermal anomalies are absent.

Figure 5. Linear correlations observed for groundwater samples collected along the Bristen Granite unit below the Maderaner Valley at ca. 9 km along the tunnel (Fig. 2). (a) SO$_4$ vs. Cl. (b) Li vs. Cl. (c) $\delta^{18}O$ vs. Cl. None of the correlations match the compositions of the samples forming the Cl peak, which is observed within the Intschi zone at ca. 10 km along the tunnel (Fig. 2c).

Figure 6. Depth-dependent porosity and vertical permeability (z-direction) distribution used to run the numerical simulations. The gray rectangular denotes the range in permeability reported for the nearby Sedrun section (Masset and Loew, 2013). Compared to the relation shown on (b), permeability in x- and y-direction were reduced by a factor of 10 to account for the steeply dipping units and nearly vertical fracture systems (Fig. 2a), suggesting that flow is directed vertically.

Figure 7. Model geometry and initially specified conductive temperature distribution corresponding to a geothermal gradient of 25 °C km^{-1} (Vernon et al., 2008).

Figure 8. Selected model output for the full model domain at steady state. (a) Upflow velocity distribution (i.e. positive z-component of the computed average linear flow vectors), suggesting that downflow (v_Z<0 m s^{-1}, lower limit of color scale) occurs at high altitude, whereas upwards directed flow zones (v_Z>0 m s^{-1}) are found beneath major valleys. (b) Cl-concentration distribution, demonstrating that water discharging into major valleys show the highest Cl-concentrations and hence experienced the longest residence times. Steady state isotherms are shown on (a) and (b) and their similarity to the initially specified temperature distribution (Fig. 7) demonstrates that the computed flow system does not cause significant thermal anomalies.

Figure 9. Simulated δ^{18}O value distribution after (a) 5,000 years, (b) 20,000 years, and (c) 100,000 years of simulation time.

Figure 10. Simulated Cl breakthrough curves for two different locations along the Amsteg section of the tunnel (Fig. 2a). (a) Cl breakthrough relating to a distance of 15 km along the tunnel where it intersects a migmatitic rock unit (Mig) below the Chrüzlistock. (b) Cl breaktrhough relating to a distance of 9 km along the tunnel where it crosses the center of the Bristen Granite unit below the Maderaner Valley.

Figure 11. Computed streamlines of meteoric water infiltrating at the upper model boundary and discharging into the tunnel along the identified upward directed flow zone between 8.5 and 11.5 km along the tunnel (Fig. 2a).

Supplementary material for on-line publication only
Click here to download Supplementary material for on-line publication only: SupportingInformation-revision.docx